Experimental and Finite Element Analysis of Fatigue Strength for 300 mm^2 Copper Power Conductor

Fachri P. Nasution[1,]

Department of Marine Technology, NTNU, Otto Nielsens vei 10, 7491, Trondheim.

Svein Sævik

Department of Marine Technology, NTNU,Otto Nielsens vei 10, 7491, Trondheim.

Stig Berge

Department of Marine Technology, NTNU,Otto Nielsens vei 10, 7491, Trondheim

Abstract

The fatigue strength of a 300 mm^2 stranded copper conductor was investigated experimentally and by finite element (FE) analysis. An analytical model was also developed and validated. Wires taken from the outer layer of the conductor were fatigue tested in tension-tension loading and compared with similar data for wire taken from a 95 mm^2 conductor. The wire cross section was deformed due to the compacting process that was applied during fabrication. When corrected for stress concentrations due to the deformation the data for the two sets of wire fell within the same scatter-band. Full scale testing was carried out in a specially designed rig with constant tensile load and reversed displacement controlled bending with a fixed curvature variation. The loading is a simulation of the loading of a power cable hanging from a floating vessel through a bellmouth. Conductors were tested in two states; dry and lubricated. A finite element model was established for the copper conductor. The model was formulated by a combination of elastic beam and beam-contact elements that included the effects of friction. The effect of local bending due to contact forces was included in the model. Two contact conditions were investigated; the point (trellis) contact between ad-

[☆1] Corresponding author Tel: +47 735 955 64

Email address: fachri.nasution@ntnu.no (Fachri P. Nasution)

jacent layers of wire and the inline contact within each layer and between the first layer (centre wire) and the second layer. The FE model was validated by a calibration test of a full scale conductor, and by sensitivity studies varying the size and the number of elements of the model. Fatigue analysis of the conductor was carried out, based on the S-N curve for individual wires. Taking into account the effects of friction and local bending, agreement was obtained between predicted and experimental fatigue strength of the conductor, for the FE model as well as the analytical model.

Keywords: Fatigue strength, copper power conductor, tension-tension mode, tension-bending mode, FE models.

---

1. Introduction

Compliant slender structures such as flexible pipes, tethers, synthetic ropes, umbilicals and flexible power cables are widely used in the offshore industry. In floating production systems for oil and gas, flexible pipes are used for transporting hydrocarbons from the wells to the production unit. Umbilicals provide energy supply (electric or hydraulic), chemical injection and signal transmission to remotely installed equipment. Flexible power cables are used in conjunction with floating units for provision of energy to installations on the sea bed, electricification of floating production systems for oil and gas, or for transmission of electrical power from wind turbines to the market (Figure 1).

The power cables that are linked to a floating unit are subjected to fatigue loading from the waves and due to the movement of the vessel in the waves. Fatigue strength needs to be verified for design. The critical section with respect to dynamic loads and fatigue will in most cases be close to the top connection point (see Figure 1 at section A-A).

A power cable generally consists of multiple conductors each representing an assembly of individual wires usually made of copper or aluminium. Figure 2a shows a typical offshore power cable for an alternating current (AC) three-phase system. One cable has usually three conductors, one for each phase. Each conductor consists of copper wires helically wound in layers around a centre (core) wire. In operation, a power cable will be exposed to gravity, hydrodynamic loading from the sea, and to forces due to movements of the vessel. The gravity will induce a mean global tension ($\bar{T}$) and mean global torque moment ($\bar{M}_T$). The forces due to movements of the floating

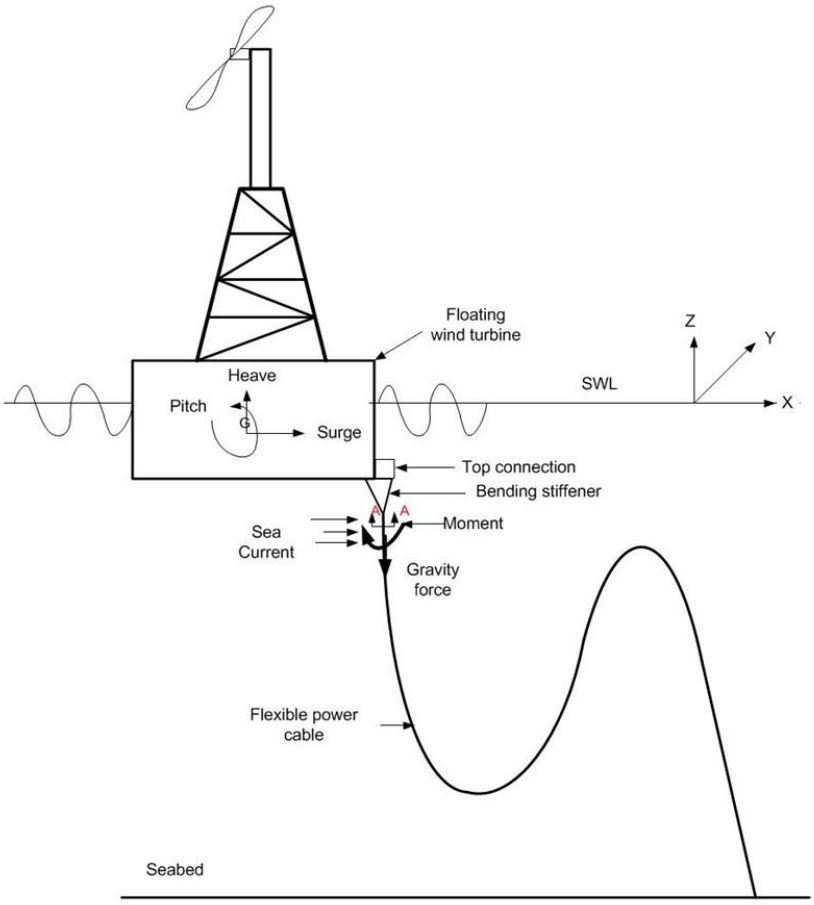

Figure 1: Flexible power cable attached to a floating offshore structure with critical section A-A closed to the top connection point.

vessel induce a dynamic tensile load (ΔT) and torque (ΔM_T) (due to heave and surge motion) and dynamic curvatures ($\Delta\beta$) (from pitch and roll motion) acting on the power cables. Mean and dynamic tension will be transferred to the wires as tension and shear forces while the dynamic bending moment will induce local bending as well as axial friction forces into each individual wire.

As shown in Figure 2b, the mean axial force ($\bar{F}_x$) in each wire is a function of the mean global tension ($\bar{T}$) and the mean global torque moment ($\bar{M}_T$). The dynamic axial force (ΔF_x) in each wire is a function of these, the corresponding dynamic quantities ΔT and ΔM_T, the dynamic curvature

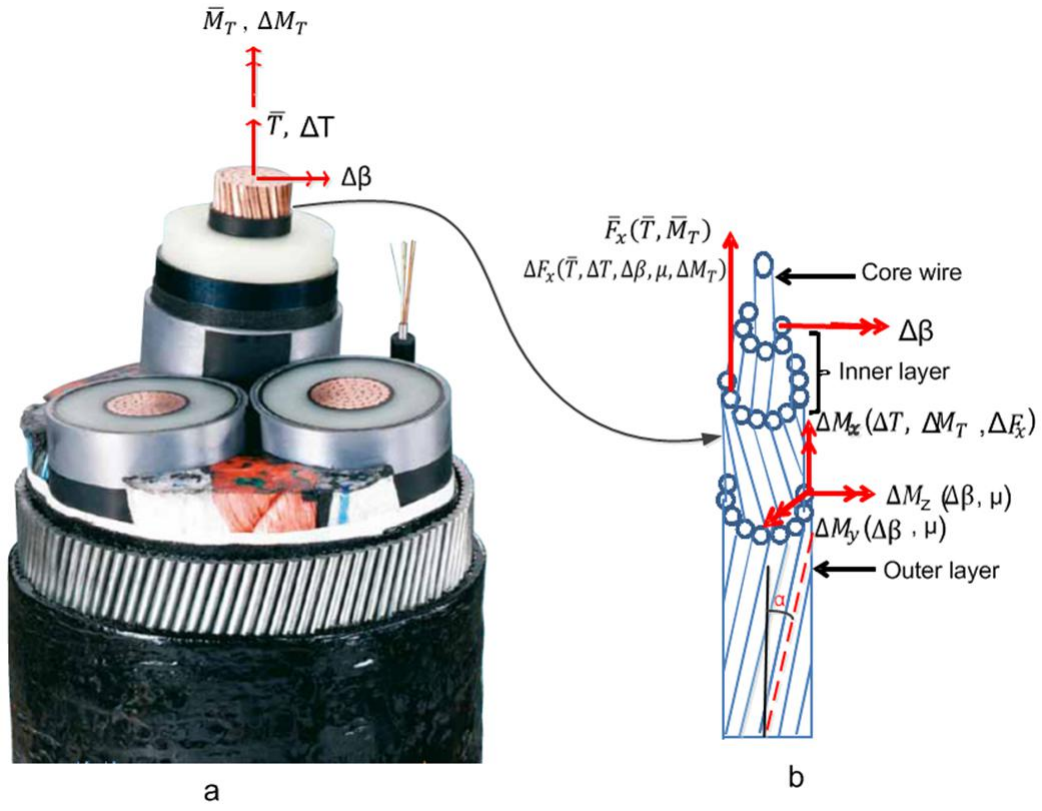

Figure 2: *a*) A typical offshore power cable for three-phase AC system using helically stranded copper conductor inside. *b*) Helically stranded copper conductor with lay angle α exposed to dynamic and static loadings.

($\Delta\beta$) and the coefficient of friction (μ) between the contact surfaces. The dynamic curvature results in local bending in each wire where ΔM_x is the dynamic torque moment about the helix tangential x-direction, ΔM_y is the dynamic bending moment about the helix bi-normal y-direction and ΔM_z is the dynamic bending moment about the principal normal vector of the helix curve.

The wires in laid conductors are stranded helically in layers which leads to contact longitudinally both within and between each layer, which is illustrated in Figure 3. Contact forces occuring within a layer and between centre (1^{st}) and 2^{nd} layer is defined as inline contact as shown in Figure 4. Contact between wires in different layers is called trellis or point contact formed at an angle θ (Figure 5) given by the lay angle α (Figure 2b). The global

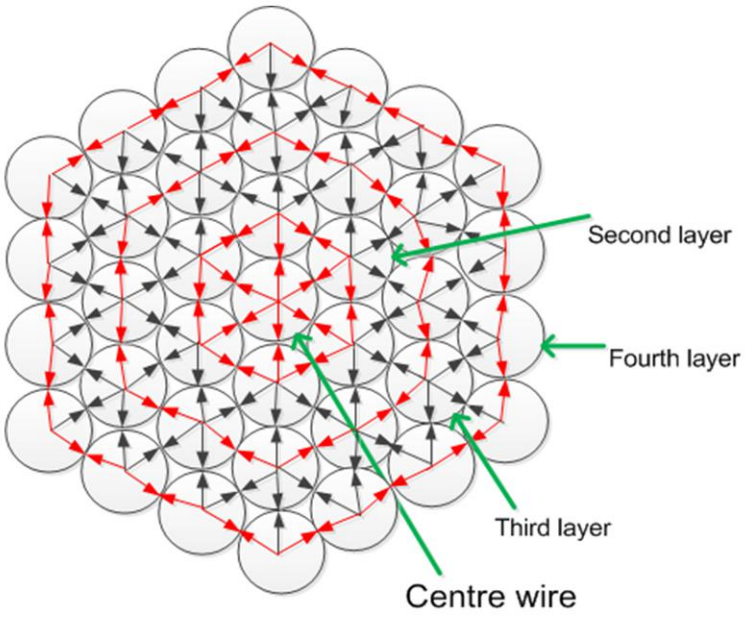

Figure 3: Plan view of a 300 mm^2 copper power conductor full cross-section. The black arrows show point contact between wires in adjacent layers and the red arrows show inline contact between wires within one layer and between 2^{nd} layer and centre wire

axial force will result in both longitudinal and transverse forces within the layer where the transverse forces will cause diameter reduction in the in-line (hoop) direction of each wire. If cylindrical bodies with diameter D_1 and D_2 are pressed together with a certain load per unit length, p, a small contact surface area will occur as shown in Figure 4.

One of the possible fatigue mechanisms in cabled structures with metal to metal contact is fretting fatigue. Fretting fatigue develops as a result of alternating stresses in combination with contact stresses on the contacting bodies.

A comprehensive literature study has been conducted with respect to models for describing fatigue and contact stresses in cabled structures. Mindlin [1] described the contact surfaces of two isotropic bodies subjected to normal and tangential loading without friction. Dong and Steidel [2] studied the contact stress conditions between layers of strands using a photoelastic technique. Johnson [3] described the Hertzian contact stresses between two solid bodies under a certain normal load. A theory of contact was developed predicting the shape of the contact area and the growth in size with increasing

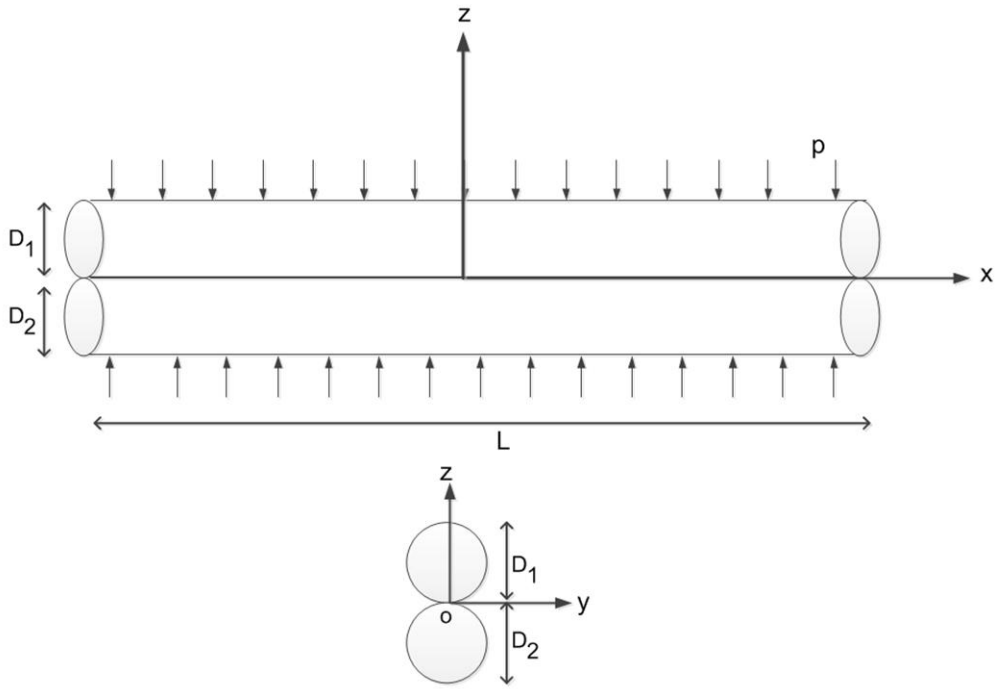

Figure 4: Inline contact between two wires within one layer and between inner layer and centre wire.

load; the magnitude and distribution of surface tractions, normal and possibly tangential forces, transmitted across the interface. Raoof [5] developed from first principles a theoretical model using axial single wire data for predicting the axial fatigue of the full cross-section steel wire rope at constant load amplitude, and was able to correlate the theoretical predictions to test data. Raoof [6] concluded that his theoretical model provided useful upper bounds for the fatigue life of cables failing at the end termination and that the termination type significantly affects the observed fatigue life. Raoof and Huang [7] proposed straightforward formulations to determine effective bending stiffness exposed to cyclic bending to a constant radius of curvature and experiencing external hydrostatic pressure. The formulations take fully into account the effect of interwire friction in the strand. Hobbs and Raoof [8] presented a model for predicting fretting fatigue due to inter-wire contact stress of steel cables under different external cyclic load conditions. They focused on helical strands in structural wire ropes. Inline and trellis contact

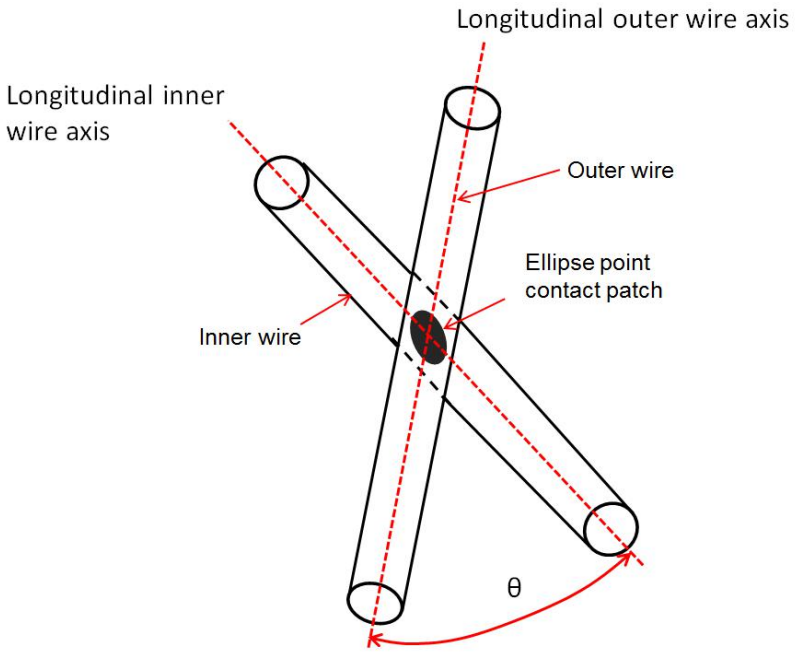

Figure 5: Trellis (point) contact occurring on adjacent layer at point contact patch.

stresses were taken into account including frictional effects. The load condition included tension and bending. Zhou, Cardou, Goudreau and Fiset [10] summarized a general fretting fatigue analysis of their previous work. They concluded that fretting behaviour and fretting fatigue strength could have an effect on conductor bending fatigue.

In 1997 Papailiou [11] presented a model under simultaneous tensile and bending loads. The model takes into account the friction and slip between layers during bending and leads to a variable bending stiffness. Hong, Der Kiureghian and Sackman [12] improved and extended Papailiou's conductor model by taking into account the layer radii, helix angle, and number of wires.

The present study focuses on copper conductors in dynamic power cables where the design is based on using protective steel armours and bending stiffeners to resist the external forces, thus limiting the tensile forces and curvatures in the conductor.

Karlsen et. al and Karlsen ([13], [14]) simulated the fatigue mechanism in dynamic power cables by dynamic testing in tension and bending. The

conclusion was that the effect of fretting on the fatigue properties was less dominant for copper conductors than for steel wires and ropes.

Recently, as reported in detail elsewhere ([16], [17]), the S-N curves for 95 mm^2 copper conductor based on nominal stress range ($\Delta\sigma$) and predicted maximum longitudinal stress range ($\Delta\sigma_{xx}$) were constructed based on axial fatigue strength of individual wires. The predicted maximum longitudinal stress range ($\Delta\sigma_{xx}$) was assessed based on the calculated SCFs (Stress Concentration Factors) for each failure location on the wire.

Moreover, bending fatigue tests of the full cross-section conductors were also conducted followed by failure investigation by Scanning Electron Microscopy (SEM) for identification of fatigue initiation location in individual wires. The observed fatigue data obtained from full cross-section testing and the stress range estimated by considering wire bending showed that the fatigue strength of the full cross-section conductors was significantly lower than the fatigue strength of individual wires tested in tension-tension.

Finite element analyses were then carried out to bridge the gap between the individual wire fatigue data and the full cross-section fatigue performance. The following main conclusions were obtained by the analysis:

1. The fatigue performance seem to be dominated by longitudinal stresses.
2. Differences found in fatigue performance between wires from different layers could be explained by differences in geometrical irregularities resulting from the manufacturing procedures.
3. No signs of fretting fatigue were seen from SEM. This was explained by the enlarged contact surfaces from the compacting procedure applied during manufacturing.
4. The fatigue performance observed from full cross-section bending fatigue testing can be predicted by FE analysis using beam and beam contact elements describing local bending and friction effects together with individual wire S-N data and layer specific SCFs.

The main objective of the present paper is to investigate the fatigue strength of a 300 mm^2 copper conductor by tests and finite element (FE) analyses and comparison with the results obtained for the 95 mm^2 conductor when using the same procedure as in [17]. The experimental work includes fatigue testing of both individual wires and full cross-section conductors including unlubricated (dry state) and lubricated conductors. Another objective of this paper was to investigate the detailed fatigue crack initiation and growth in individual wires using Scanning Electron Microscopy (SEM).

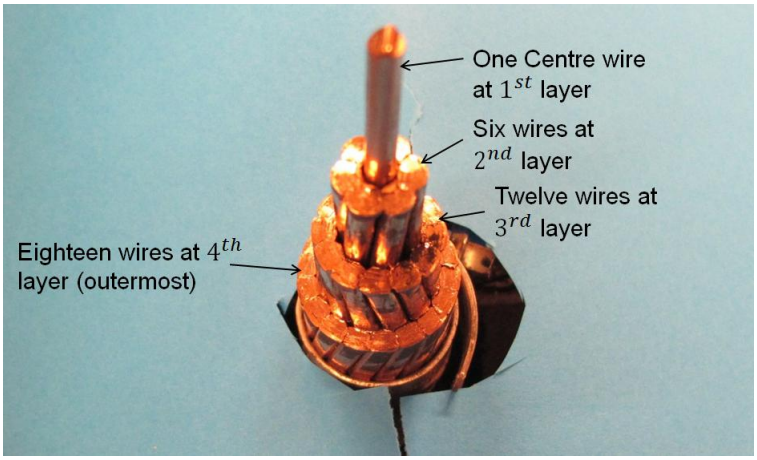

Figure 6: A photo showing the cross section of a 300 mm^2 copper power conductor.

2. Experimental Tests

2.1. General

The specimens used in this work were taken from a 300 mm^2 copper conductor (ETP copper), designated by the UNS C11000 series. The definition of ETP copper is related to copper purity of at least 99.95% and characterized by a very high electrical conductivity and ductility. The conductor cross section consisted of 37 wires, each with a nominal diameter of 3.21 mm and a cross section area of 8.11 mm^2. Based on measurements obtained from friction tests, the coefficient of friction for unlubricated conductors was found to be 0.2 [16], whereas for the lubricated case the coefficient of friction was found to be 0.02.

A centre wire is followed by six, twelve and eighteen helically wound wires in three layers as shown in Figure 6. The centre wire counted as the 1^{st} layer. The pitch lengths were measured to be 265, 285 and 295 mm for 2^{nd}, 3^{rd} and 4^{th} layers, respectively. When using the right hand lay rule the obtained lay angles were found to be $+4.33^o$, -8.03^o and $+11.56^o$, respectively, for the 2^{nd}, 3^{rd} and 4^{th} layer.

During fabrication each conductor is compacted radially to optimize the cross section. The compacting process leads to plastic deformations such as ovalisation of the wire cross section due to trellis contact.

2.2. Fatigue Testing of Individual Wires

Wires were taken from the outer (4^{th}) layer of the conductor. Due to the opposite lay angles of the helical layers, the surface irregularities from the compacting were found to be periodic with a wavelength of approximately 10 mm, as shown in Figure 7. The modulus of elasticity (E) for copper was taken to be 115 GPa [14]. The fatigue strength of individual wires could be dependent on whether the wire was taken from the centre, inner or outer layer (4^{th} layer) of the copper conductor. The test program only included wires from the outer layer.

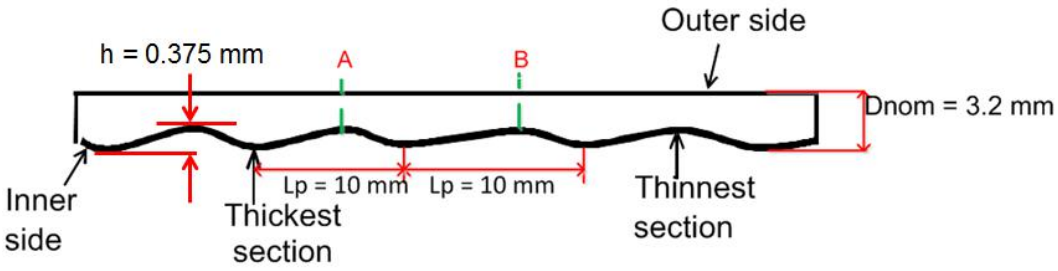

Figure 7: Geometrical surface of outer layer having plastic deformations found to be periodic with a wavelength of approximately $L_p = 10$ mm.

The wires were cut, straightened and terminated at the ends using aluminium tubes filled by high strength glue, see Figure 8.

The surface irregularities were found to be most significant for the outer layer as indicated in Figure 7. The thickness at points on thin and thick sections of the wires was measured by a digital caliper in order to obtain the statistical characteristic values such as mean value and standard deviation. The mean thickness reduction of outermost wire was 0.375 mm with a coefficient of variation (COV) of 0.027.

Three wires from the outer layer were tension tested to obtain a stress-strain curve. Stress-strain curves of the straightened outer wires taken from 95 and 300 mm^2 conductor are shown in Figure 9. The yield strength of the copper is commonly defined as the stress resulting in 0.2 % residual strain. The curves were used to establish the yield plateau for the wires. There was no significant variability of stress-strain curves among the wires that were

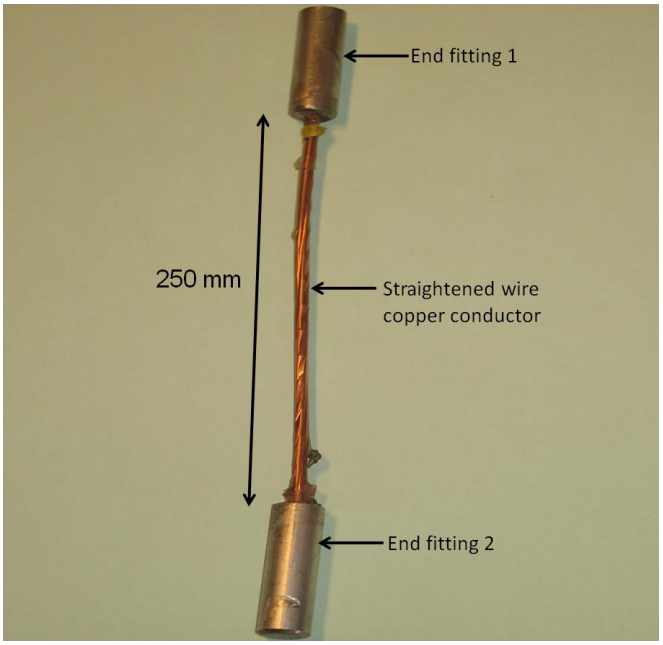

Figure 8: Straightened simple wire for fatigue tests in tension-tension mode.

tested. The results show that the yield strength of individual outer wires taken from the 95 mm^2 conductor is lower than for the wires taken from 300 mm^2 conductor.

The wire specimens were fatigue tested in constant amplitude axial tension with stress-ratio R = 0.1 and loading frequency of $f = 2\ Hz$. The loading frequency was limited by the actuator response. Three levels of nominal stress range ($\Delta\sigma$) were applied: 130, 160 and 190 MPa. The nominal stress range was based on a cross section of 8.11 mm^2 corresponding to a nominal diameter ($D_{nominal}$) of 3.21 mm. The load was applied using a standard servo-hydraulic testing machine in load control, see Figure 10.

Detailed listing of the test results is found in Table 1. Wires that failed at the end termination were considered invalid, and were not included in further analysis.

As previously reported ([16]-[17]), S-N curves based on nominal stress range ($\Delta\sigma$) have been constructed based on the fatigue tests of wires taken from 95 mm^2 copper conductor.

Figure 11 displays the data for 300 mm^2 compared to the corresponding data for wires taken from the 95 mm^2 conductor based on the nominal stress

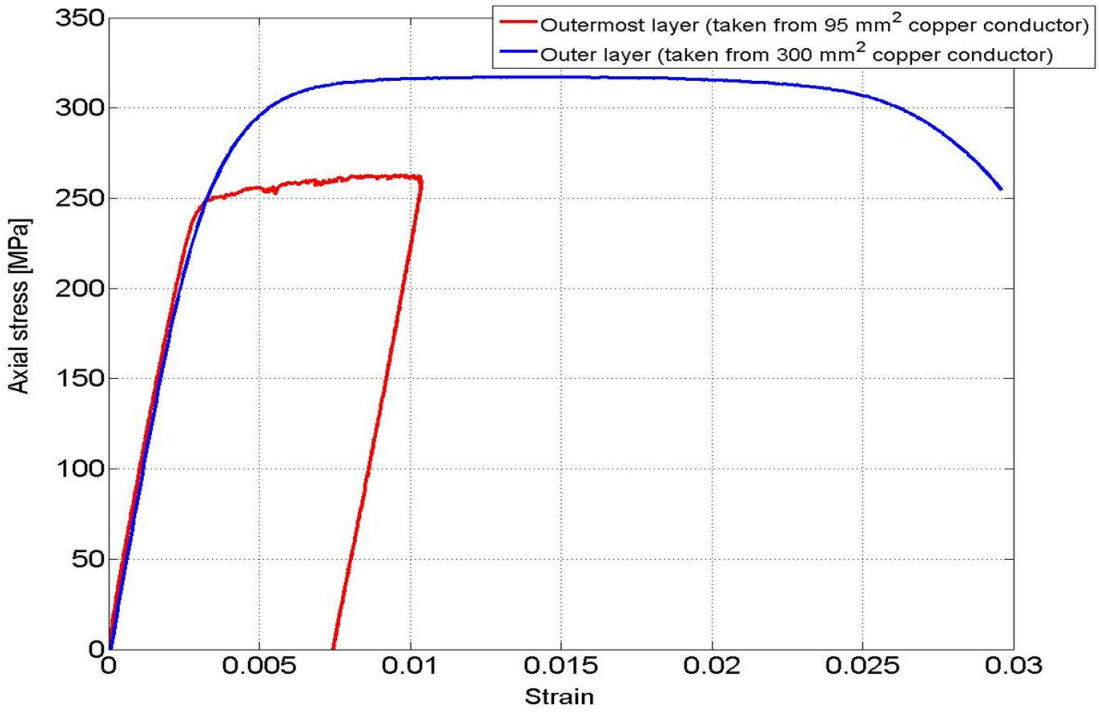

Figure 9: Comparison average of stress-strain curve between individual outer wire taken from 95 and 300 mm^2 copper conductor.

ranges $\Delta\sigma$. The blue line is the mean life S-N curve for wires from 95 mm^2 conductor. The upper and lower bounds of the S-N data are based on the plus/minus two standard deviations scatter band. The results show that the wires of 300 mm^2 have longer fatigue lives than the wires from 95 mm^2 copper conductor.

The maximum longitudinal stresses (σ_{xx}) of individual wires were then assessed based on the measured irregularities and FE analysis to obtain the SCFs relative to nominal stresses.

The calculation of SCFs was carried out using the finite element software ABAQUS. The model is symmetric and covers both the thickest and thinnest sections of the wire shown in Figure 12. The SCF model was constructed by 9100 elements using reduced-integration elements type (C3D8R) in stress/displacement analyses. The model represents the point contact patch from section A through B illustrated in Figure 7 (at section A-B). The model is subjected to static tensile stress of 100 MPa at section B and the

Figure 10: Test rig setup for fatigue test of an individual wire in tension-tension mode with both ends clamped against rotations.

boundary condition is fixed at section A in the X-direction. The dimensions on the model was average values obtained from measurements as displayed in Figure 12.

The maximum SCF for axial loading, $SCF_{(a)}$, occurred at the thinnest section of wire and was calculated as:

$$SCF_{(a)} = \frac{\sigma_{peak}}{\sigma_{nominal}} \tag{1}$$

where σ_{peak} represents the maximum stress and $\sigma_{nominal}$ is the nominal applied axial stress. Figure 13 shows that the mean SCF for wires based on Eq. (1) is 1.08 and located at the root (junction) between the thickest and thinnest part. This is significantly smaller than the SCF of wire taken from 95 mm^2, found to be 1.238 in [17].

The S-N data of outer wires based on the maximum stress range $\Delta\sigma_{peak}$ is shown in Figure 14. The slope parameter for the mean life S-N curve of 95 mm^2 conductor is $m = 8.41$. The S-N data for the two sets of wire taken from 300 mm^2 and 95 mm^2) appear to fall in the same scatter-band.

Table 1: Fatigue data for nine outermost wires failed at thinnest section.

No	$\Delta\sigma$	No. cycles to failures [cycles]
1	130	6799803
2	130	8212235
3	130	8878805
4	160	2482476
5	160	2586506
6	160	3176399
7	190	706421
8	190	728768
9	190	831666

2.3. Fatigue Bending Testing of Full Cross-Section Copper Conductor

Bending fatigue tests of the full cross-section copper conductor were conducted. The intention of the test was to simulate the loading of a conductor hanging from a floater through a bellmouth (bending restrictor) and subjected to the motions of a floating structure. In this test the bending was applied in one plane.

A full cross-section conductor with free span length 2680 mm and cross section 300 mm^2 is shown in Figure 15. A schematical sketch of the experimental set-up is shown in Figure 16. The test rig is composed of two outer external steel frame structures, two bellmouths with constant radius of curvature, two die springs to provide tension and a beam that is driven by a hydraulic actuator. The test is controlled and monitored by extensive instrumentation such as two load cells, two LVDTs, closed-loop control system, etc. and a computerized data acquisition system. The bellmouths were designed to induce deformation controlled reversed bending to a fixed curvature in the specimen.

The conductor was axially pre-tensioned by die springs attached to each end with a constant tensile load of 30000 N (σ = 100 MPa). Both ends were further connected to the outer external frames 1 and 2, where the cyclic bending motions were induced by prescribed displacement of the actuator piston. Transverse forces were applied at midpoint of the bellmouth. The

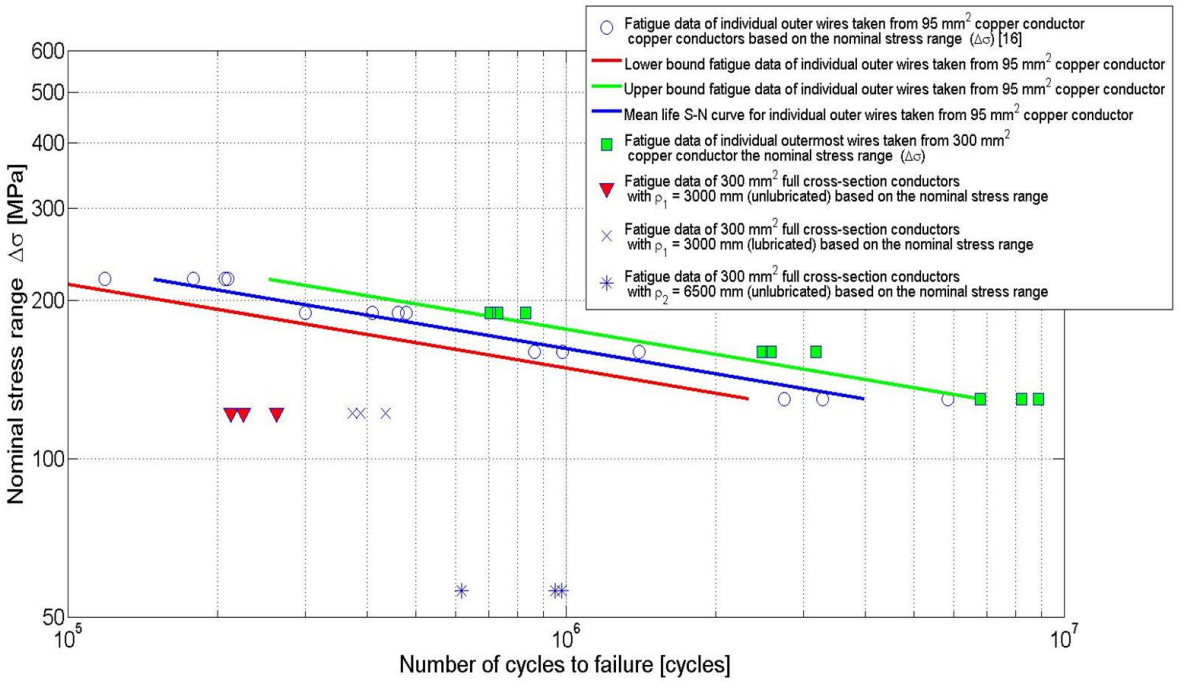

Figure 11: S-N fatigue data of individual outer wires taken from 300 mm^2 power copper conductor compared to S-N data of individual wires taken from 95 mm^2 in tension-tension mode based on the nominal stress range $\Delta\sigma$.

nominal stress was calculated as outer fibre stress from elementary beam theory:

$$\sigma_{nom} = \frac{F_{axial}}{A_{full}} \pm E\frac{R_{nominal}}{\rho} \tag{2}$$

where E is the modulus of elasticity of copper taken as 115 GPa [14]. ρ is the radius of curvature $[mm]$ and F_{axial} is the constant applied tensile force (30000 N) acting from die springs, A_{full} defined as cross section area 300 mm^2 and $R_{nominal}$ is the nominal individual wire radius, taken as 1.6 mm. It is noted that the above equation excludes the effect from local bending and friction. For more details of the test set-up and the test procedures see ([16], [17]).

Table 2 shows the fatigue test data for the nine full cross-section conductors that were tested. Unlubricated and lubricated copper conductors were tested.

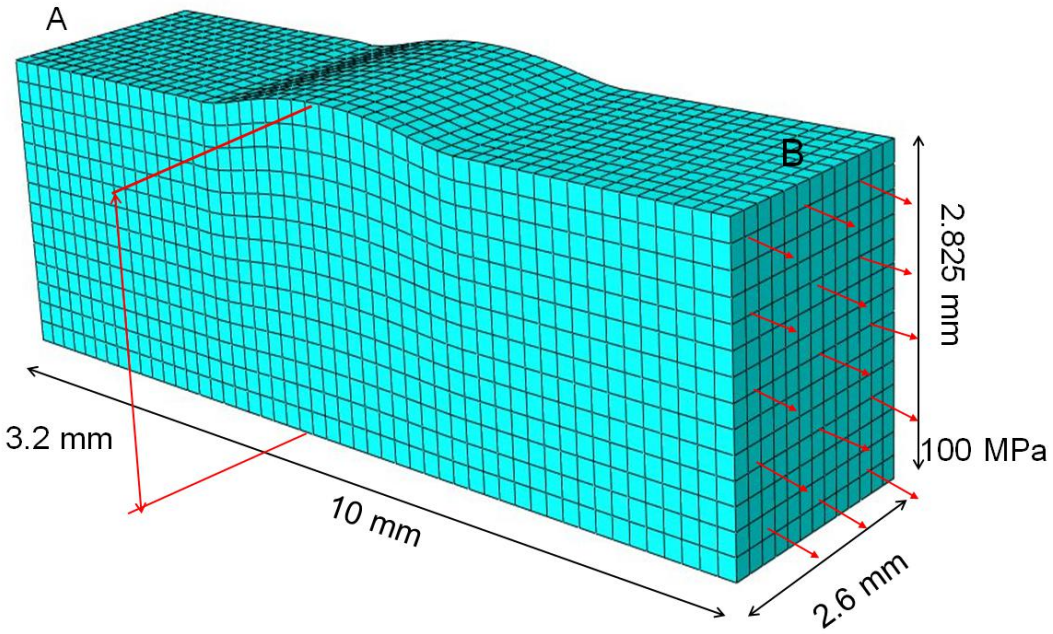

Figure 12: A contact point patch model represents the thickest and thinnest parts of outermost wire in 3D view, as representation section A-B in Figure 7.

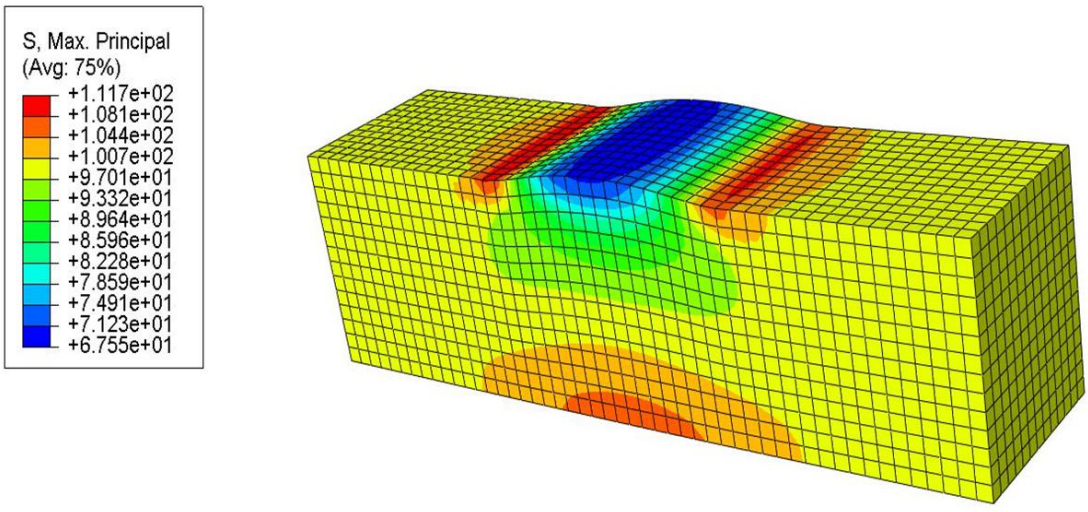

Figure 13: Stress variations on the contact point patch of outermost wire in 3D view.

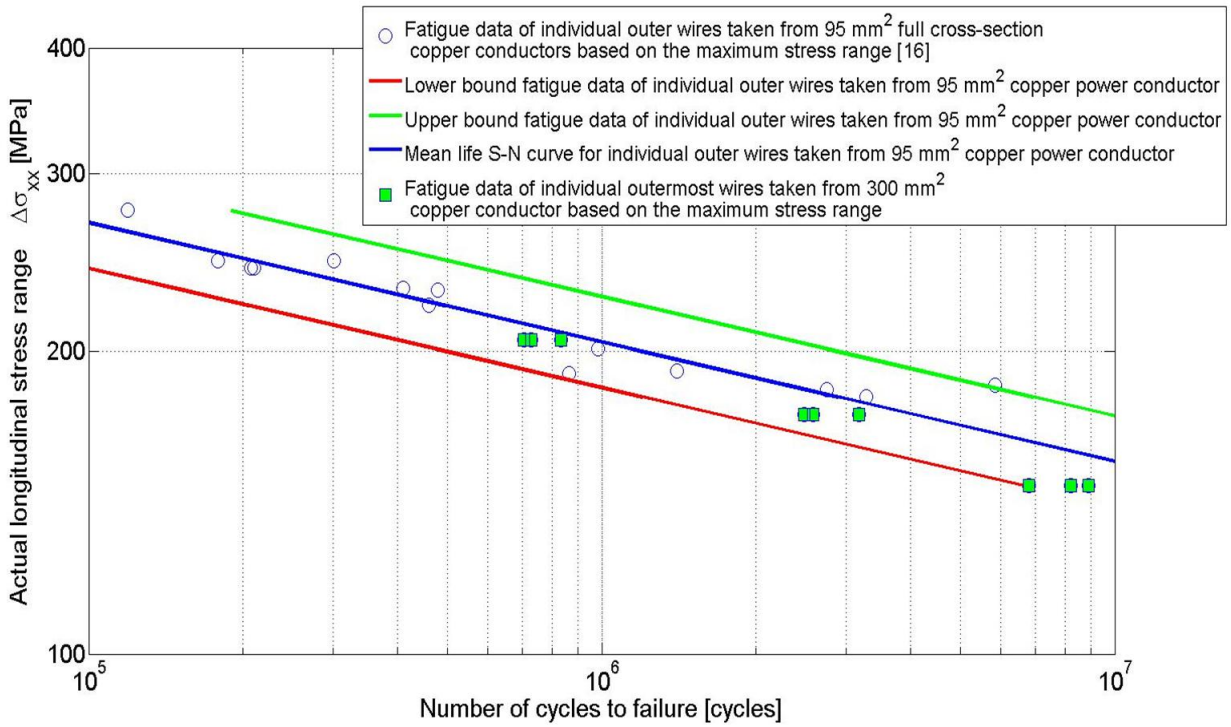

Figure 14: S-N fatigue data of individual outermost wires taken from 300 mm^2 copper conductor compared to S-N curve of individual wires taken from 95 mm^2 in tension-tension mode based on maximum stress range $\Delta\sigma_{xx}$.

The fatigue bending test data based on nominal stress range from Eq. (2) is shown in Figure 17. It is clearly demonstrated that the fatigue lives for lubricated conductors based on nominal stress is longer compared to unlubricated (dry state) conductors. The fatigue failures for dry state conductors were found in the 2^{nd} and 3^{rd} layers. However, it was difficult to determine in which layer the first fatigue failure occurs. The fatigue failures for lubricated conductors took place only in the 2^{nd} layer. Furthermore, on the same basis of nominal stress the fatigue strength of individual wires is larger than that of full scale conductors, indicating that local bending, friction and possibly fretting effects are significant (see Figure 7).

2.4. Fractography of wires tested in full cross-section

Fractographic investigation of wires taken from the full cross-section conductors that had been fatigue tested in bending was conducted using Scan-

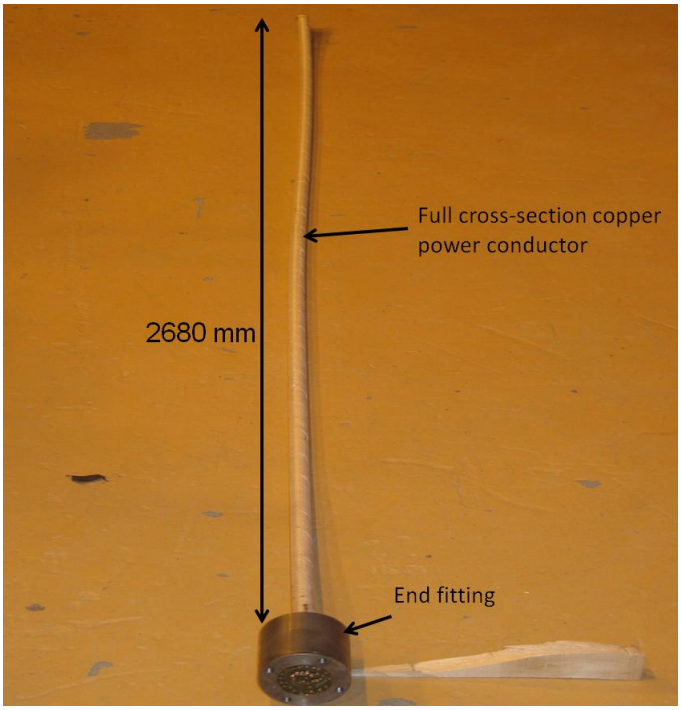

Figure 15: A full cross-section specimen of a 300 mm^2 power copper conductor.

ning Electron Microscopy (SEM). The purpose of the investigation was to identify the location of fatigue initiation relative to orientation of each wire in the conductor. Of particular interest was a possible correlation with trellis points, or deformed surface from the compacting processes.

By dissection of the conductors, a large number of individual wire failures were found. All fatigue failures were located in the 2^{nd} and 3^{rd} layers, counting from the centre wire as the 1^{st} layer, in the section that had been subjected to bending inside the bellmouth.

The orientation of the fracture surfaces relative to the axis of the conductor could be identified by the oxidised markings of the trellis points, herein referenced as "inside" pointing towards the axis of the conductor and "outside" pointing outwards.

Due to the large number of failed wires and the general state of the conductors during dissection it was not possible to identify the orientation and the exact location of the failures relative to the bending axis.

Fractography was carried out, to identify the location of fatigue initiation

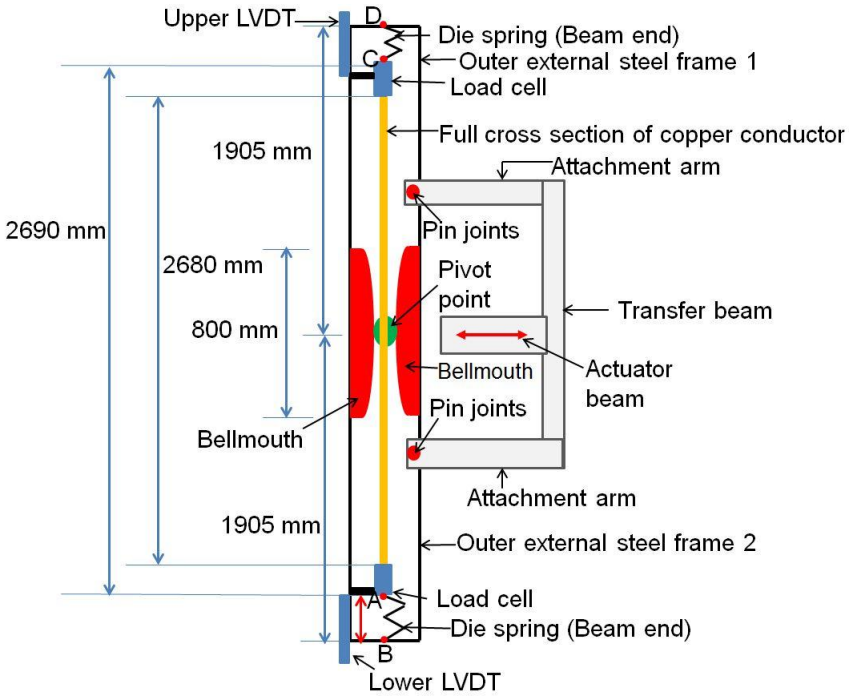

Figure 16: A principal sketch of cyclic bending fatigue rig for full cross-section copper conductor at initial condition (adopted from [16]).

on the wires. The 23 failed wires were prepared, taken from unlubricated conductors that had been subjected to an alternating radius of curvature of 6500 mm and 3000 mm. The failed wires were assembled by mounting to aluminium block shown in Figure 18 for SEM investigation. The oxidised trellis points are clearly visible on the surfaces of the specimens.

The mode of loading in the tests was fully reversed displacement bending (load ratio R = -1) with static axial stress. Some of the fracture surfaces were thus deformed (smeared) due to crack closure. However, most of the specimens had features that could be observed, for identification of the location of fatigue initiation and crack growth direction.

In Figure 19 is shown a fracture surface from a specimen that had been tested with a radius of curvature $\rho_1 = 3000\ mm$. The arrow points at the location of crack initiation, which is at the outside (relative to conductor axis), directly under a trellis point.

Figure 20 shows at larger magnification the initiation location. Part of

Table 2: Full cross-section copper conductor parameters and the fatigue bending test results.

No	$\Delta\sigma$ [MPa]	σ_{xx} [MPa]	Radius of curv. [mm]	No. of cycles to failure [cycles]	Remark	Failure position (layers)
1	122	161	3000	212644	unlubricated	2^{nd}-3^{rd}
2	122	161	3000	225244	unlubricated	2^{nd}-3^{rd}
3	122	161	3000	262394	unlubricated	2^{nd}-3^{rd}
4	56	128	6500	617474	unlubricated	2^{nd}-3^{rd}
5	56	128	6500	951059	unlubricated	2^{nd}-3^{rd}
6	56	128	6500	980782	unlubricated	2^{nd}-3^{rd}
7	122	161	3000	387178	lubricated	2^{nd}
8	122	161	3000	372636	lubricated	2^{nd}
9	122	161	3000	434643	lubricated	2^{nd}

the surface of the wire is also seen (lower section of the photo), with the flattened part of the trellis point.

Figure 21 shows a section close to the centre of the wire. Below the arrow, and also in other parts of the image are shown striations with a spacing of the order of 1 μm, indicating crack growth in the direction of the arrow. Close to the initiation location no features of crack growth could be observed, due to smearing of the surface.

The same pattern was found on all specimens that were subjected to SEM. Fatigue initiation in the 2^{nd} and 3^{rd} layers had taken place from the outside of the wire relative to the conductor axis, under a trellis point.

No indication of fretting was found (scale, stick-slip transition). This is in line with the observations reported by Karlsen [14]

2.5. Calibration Test

A tensile test with a 300 mm^2 conductor was carried out for calibration of the FE model.

A copper power conductor with free span length 1000 mm was mounted in a servo-hydraulic test machine. On each individual wire of the outer

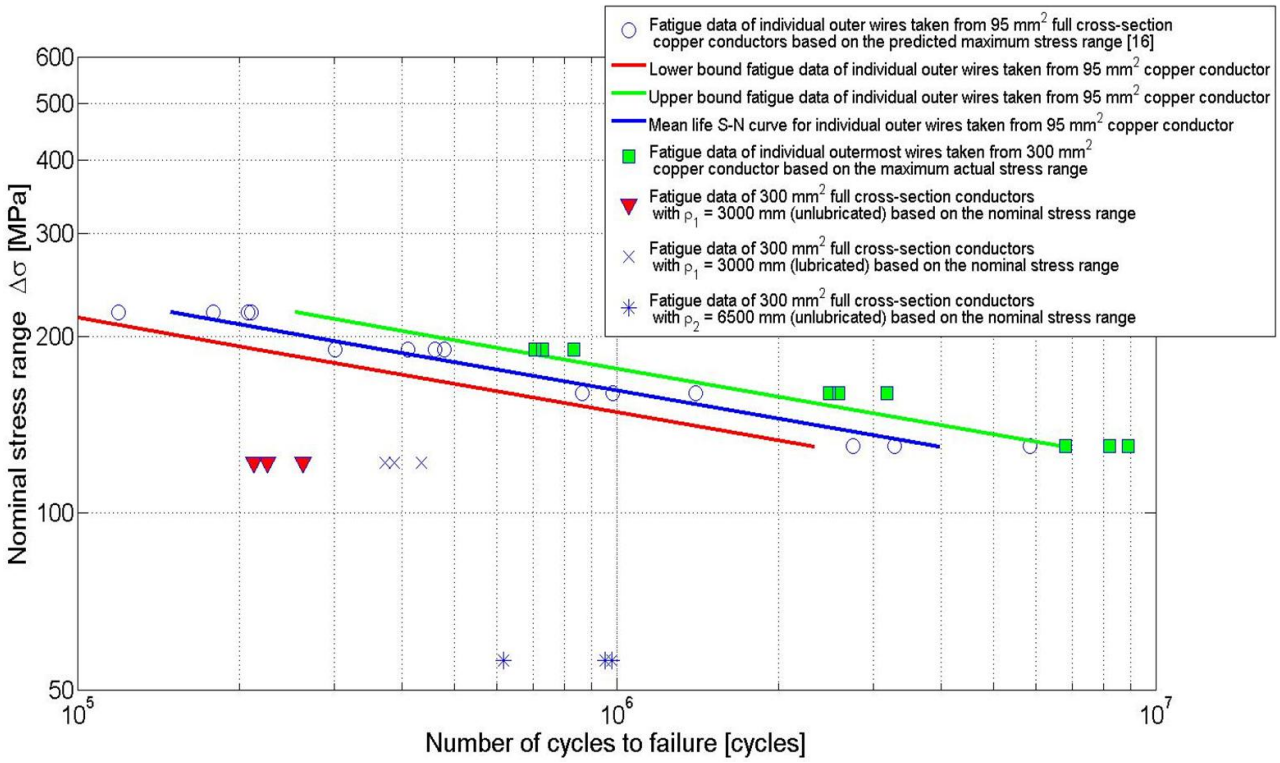

Figure 17: Fatigue test data of full cross-section conductors and individual outermost wires based on fatigue test data of individual wires taken from 95 mm^2 in tension-tension mode using nominal stress range $\Delta\sigma$.

layer strain gages were attached for measuring axial strain. In addition, the specimen was equipped with an extensometer for monitoring the nominal axial strain of the conductor as shown in Figure 22. The results are presented and discussed in Section 5.1.

3. Analytical Calculation of Stresses

3.1. Components of Stress

A power conductor is exposed to static and dynamic tension in combination with dynamic curvature. The conductor consists of n wires including the centre wire and m layers of helical wires all having same diameter d, area A and Youngs modulus E. Each layer consists of n_i wires with layer radius R_i and lay angle α_i.

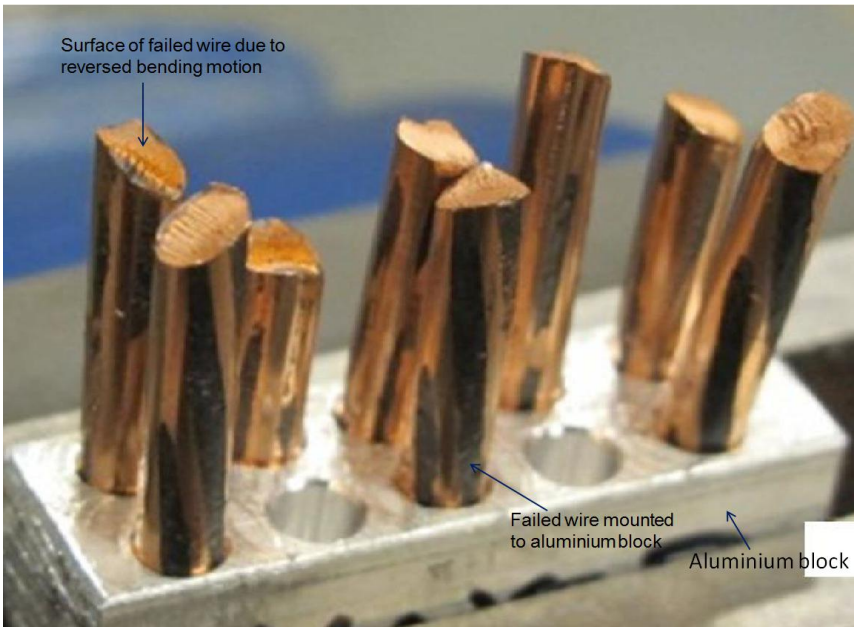

Figure 18: The failed wires taken from full cross-section conductors, mounted for SEM investigations.

The longitudinal stress range can be decomposed into:

$$\Delta\sigma = \Delta\sigma_T + \Delta\sigma_{tc} + \Delta\sigma_{nc} + \Delta\sigma_f \tag{3}$$

where $\Delta\sigma_T$ is the stress range from dynamic tension, $\Delta\sigma_{tc}$ is the stress range from transverse curvature of the wire, $\Delta\sigma_{nc}$ is the stress range from normal curvature of the wire and $\Delta\sigma_f$ is the stress range from friction. In this case, the maximum longitudinal stress is at the outer fibre of the conductor . Therefore, the stress range due to transverse curvature is ignored.

3.2. Stress Range from Dynamic Tension

Using the principles outlined in [18] and neglecting radial deformations, the axial stiffness of the conductor can be calculated as:

$$EA_{full} = EA\left(1 + \sum_{i=1}^{m} n_i \cos^3 \alpha_i\right) \tag{4}$$

where EA is the axial stiffness of each wire, n_i is the number of wires in layer i and α_i is the lay angle of layer i. When exposed to dynamic tension, this

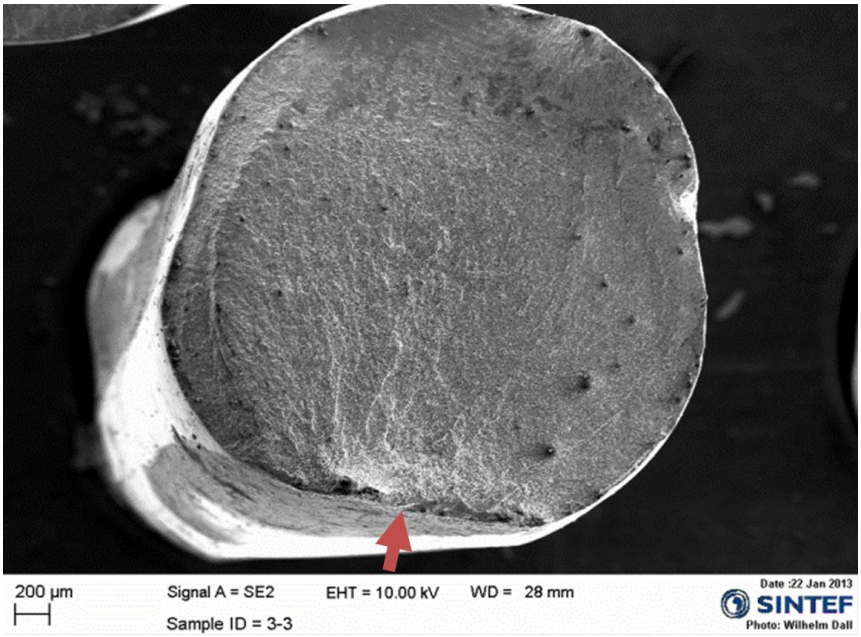

Figure 19: Fracture surface from 3^{rd} layer of a conductor that had been fatigue tested with radius of curvature $\rho_1 = \pm$ 3000 mm.

will give a stress variation in each wire as,

$$\Delta\sigma_T^i = E\cos^2\alpha_i \frac{\Delta T}{EA_{full}} \tag{5}$$

3.3. Elastic Bending Stresses

For the dynamic bending moment about the helix bi-normal axis (M_y) shown in Figure 23, the bending stress range for small lay angle α_i can be obtained by an approximate expression [20].

$$\Delta\sigma_{nc} = R_{nominal}E\cos^2\alpha_i\cos 2\alpha_i\Delta\kappa\cos\Psi \approx R_{nominal}E\Delta\kappa\cos\Psi \tag{6}$$

$\Delta\kappa$ is the curvature range and Ψ is the polar coordinate angle defining the helix position.

3.4. Friction Stress

Using the principles outlined in [18], the friction stress range can be calculated as the smallest stress range obtained by either of the plane surfaces

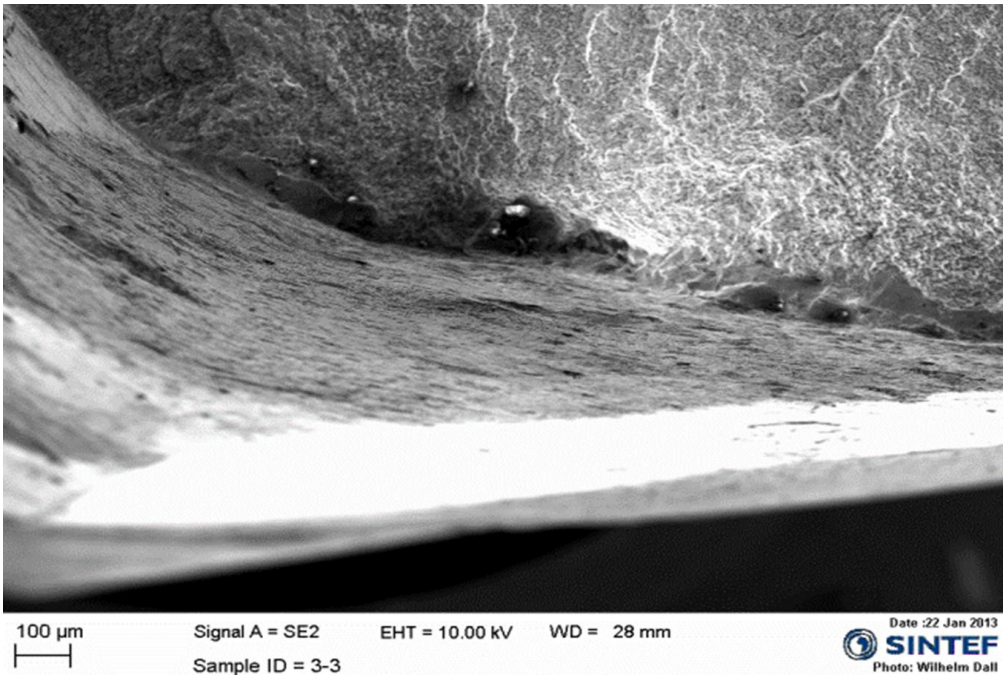

Figure 20: Enlarged section of Figure 19. Location of fatigue crack initiation.

remain plane solution and the maximum that can be allowed due to the friction between the interfaces as:

$$\Delta\sigma_f^i = min\left(E\cos^2\alpha_i R_i \Delta\kappa, \frac{\pi R_i \tau_i}{\sin\alpha_i A_i}\right) \tag{7}$$

The latter expression is simply a result of integrating the available friction force per unit length τ_i along a quarter pitch length multiplied by 2 and divided by the wire area A_i.

In order to obtain the available friction force for the layer i the contact pressure at all interfaces are needed. Based on the observations from full scale fatigue testing a simplified approach is used, neglecting the in-layer contact forces, i.e. only the contact forces on the outside and inside of the layer are considered. First the strain resulting from the mean static tension T is defined as a global parameter:

$$\epsilon_c = \frac{T}{EA_{full}} \tag{8}$$

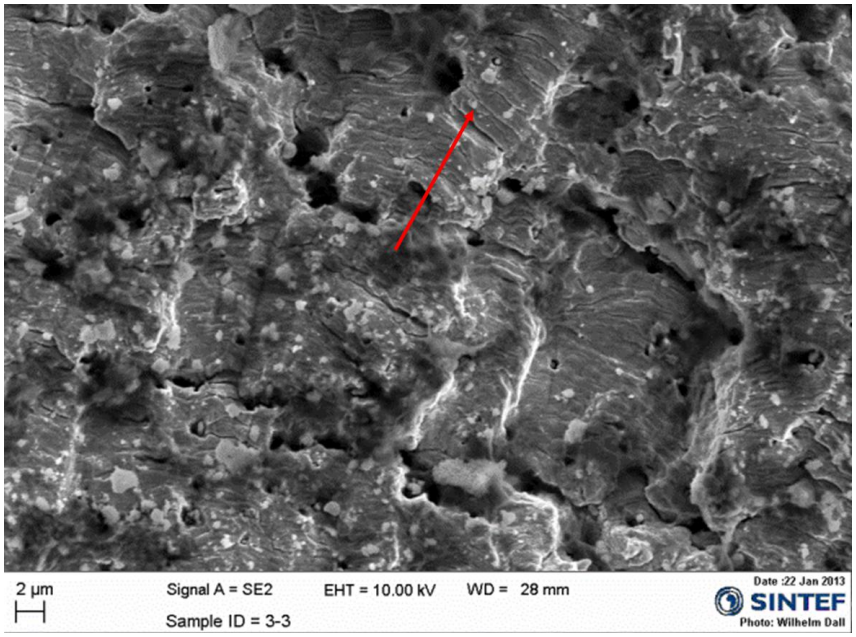

Figure 21: Fracture surface close to centre of the wire, direction of fatigue crack growth.

and

$$\tau_i \cong E\epsilon_c\mu \left(\sum_{j=i+1}^{m} \frac{n_j A_j \cos^2\alpha_j \sin^2\alpha_j}{n_i R_i} + \sum_{j=i}^{m} \frac{n_j A_j \cos^2\alpha_j \sin^2\alpha_j}{n_i R_i} \right) \quad (9)$$

where μ is the coefficient of friction.

4. Finite Element (FE) Model for Full Cross-Section Copper Conductor

4.1. General

UFLEX3D is a finite element tool for 3D stress analysis of umbilicals [21], however, including beam stresses due to internal pressure, external pressure, tension, torsion and bending loads.

The conductor was modelled using elastic beam elements for all wires with a constant elastic bending, axial and torsion stiffness.

The conductor model was 1000 mm long including one centre wire (1^{st} layer), six wires for 2^{nd} layer, twelve wires for 3^{rd} layer and eighteen wires for

Figure 22: A calibration test for 300 mm^2 copper conductor.

outermost layer (4^{th} layer) as shown in Figure 24. The model was meshed with 400 elements per wire in the longitudinal direction.

The contact elements include four parts, namely:

1. Point contact elements between 2^{nd} and 3^{rd} layers and between 3^{rd} and 4^{th} layers.
2. Inline contact elements, within layers.
3. Inline contact between centre wire (1^{st} layer) and 2^{nd} layer.

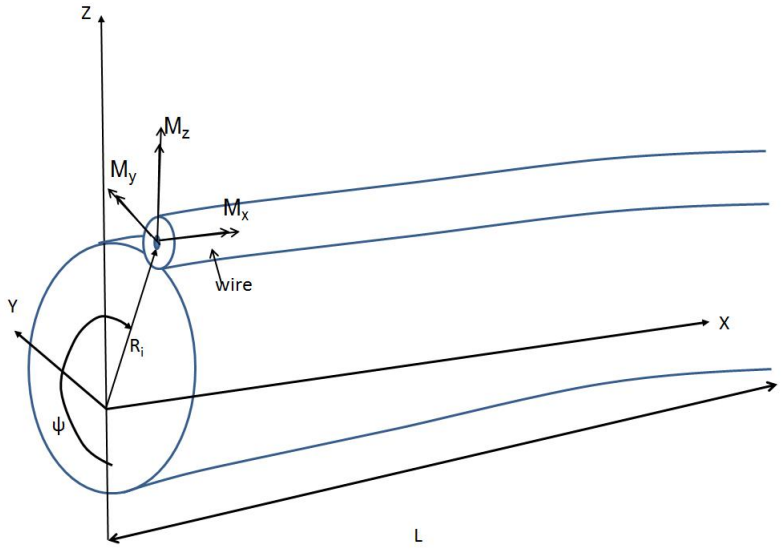

Figure 23: A simple power conductor model.

4. Contact between the outer layer of the conductor and the bend surface (i.e., bellmouth).

The bellmouth was modeled as a geometrical surface, where a penalty stiffness is applied during wire-surface contact. No friction is included in this contact element.

The wire to wire contact elements were given an elastic stiffness in the normal direction whereas friction was treated by an elastic-plastic model using a stick-slip displacement parameter.

The normal stiffness need to be established based on a compromise between numerical accuracy and stability. A contact model and procedure for calibrating was presented in [17] based on:

1. Axial stiffness testing and the use of calibration factors C_{in} and C_{po} for inline contact and point contact, respectively.
2. The associated stick-slip displacement Δ that allows describing the plane surface remain plane condition is an approximate way.

Inline contact, f_{inline}, is defined in [17]

$$f_{inline} = C_{in} \frac{E b_{eq}}{R} \delta_n \tag{10}$$

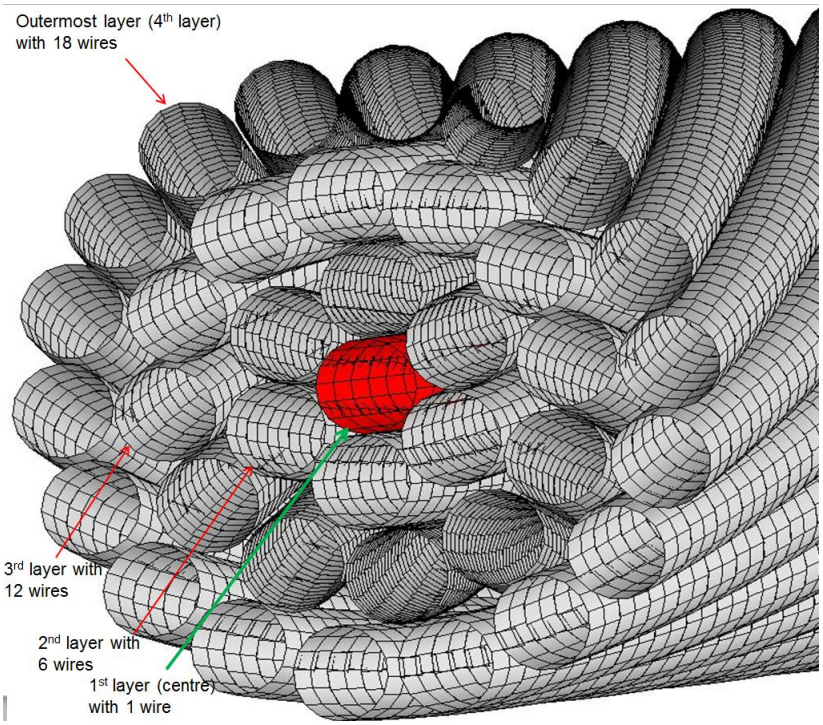

Figure 24: Complete 3D model of a 300 mm^2 full cross-section power copper conductor.

where C_{in} is a calibration factor for inline contact, δ_n denotes the normal contact displacement and b_{eq} is established from the cross section of a wire A taken as 8.11 mm^2 and the wire radius $R_{nominal}$ taken as 1.6 mm

The point contact force, F_{point}, is defined in [17].

$$F_{point} = C_{po}\frac{A_c E}{2r}\delta_n \tag{11}$$

where A_c is taken to be the projected area between two wires from adjacent layers.

The associated stick displacement is defined based on an approximate description of the plane surfaces remain plane condition [17]. The stick displacement for inline and point contact were defined by:

$$\Delta_{inline} = \frac{nR^2 f_{inline}\mu}{\left(\frac{1}{F_{tol}} - 1\right) EA\sin^2\alpha} \tag{12}$$

$$\Delta_{point} = \frac{nR^2 F_{point}\mu}{\left(\frac{1}{F_{tol}} - 1\right) L_p E A \sin^2\alpha} \tag{13}$$

where n is the number of interfaces sharing the interaction process, F_{tol} denotes the allowable tolerance for stick relative displacement and L_p is the length between contact points (see Figure 7).

In order to perform the fatigue calculation, this has to be performed in two steps and based on the maximum longitudinal stresses (σ_{xx}) given as:

$$\sigma_{xx} = SCF_{(a)}\sigma_{xa} \tag{14}$$

where σ_{xa} represents the nominal axial stresses and SCF_a denotes stress concentration factor for axial loading. The steps are:

1. Calculate the fatigue damage representative for the sections away from the point contacts (away from the thinnest section) by using 1.0 for all SCFs in all layers.
2. Calculate the fatigue damage at the point contacts having the thinnest sections by using the data for the stress concentration factors, $SCF_{(a)}$, using the same procedure as reported previously in [17].

For the tension-bending model, the SCFs in the weak (y) and strong (z) directions are neglected since insignificant ovalisation was noted in the wires.

4.2. Tension-Bending Model

FE analyses were carried out for the conductor model subjected to reversed bending loads over the bellmouth where both ends were axially pretensioned by end beams with a constant tensile force of 30000 N. The test setup had a model length of 3000 mm. However, the full detail FE model length was truncated to 2000 mm (approximately seven pitches) due to computing limitations. Two radii of bellmouth curvature were investigated $\rho_1 =$ 3000 mm and $\rho_2 = 6500$ mm at a constant tension of 30000 N according to the test parameters.

Figure 25 presents the complete FE model of full cross-section copper conductor with model length (L) at the initial condition including the bending rig. The end beams simulating the die springs were connected to the outer external tubular frames 1 and 2, where the cyclic bending is induced by prescribed displacement of the beam actuator. This motion is then transferred to the external frames by means of the transverse beam and the attachment

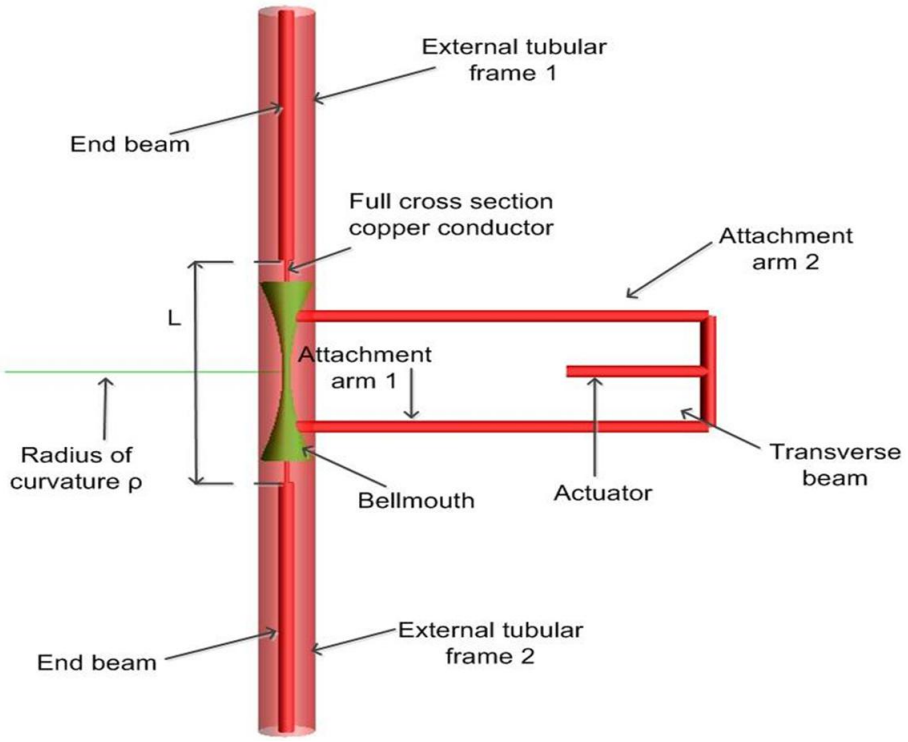

Figure 25: FE tension-bending model for full cross-section copper conductor at initial condition including bending rig (adopted from [17]).

arms at 1 and 2. Two different FE models of the conductor were established to check the sensitivity with respect to the model length and number of meshes, see Figure 26.

5. FE Results

5.1. Calibration

Figure 27 shows the correlation of results obtained from the procedure described in Section 4 above. The deviation between the tests and FE model is about 15%. Noting that numerical stability was significantly challenged when trying to fit the test data with the numerical model this was considered acceptable. The contact calibration factors for inline (C_{in}) and point contact (C_{po}) are obtained from Eqs. (10) and (11), respectively and summarised in Table 3. The C_{in} for the 3^{rd} and the outermost layers are less than for the other layers and was found as a compromise considering:

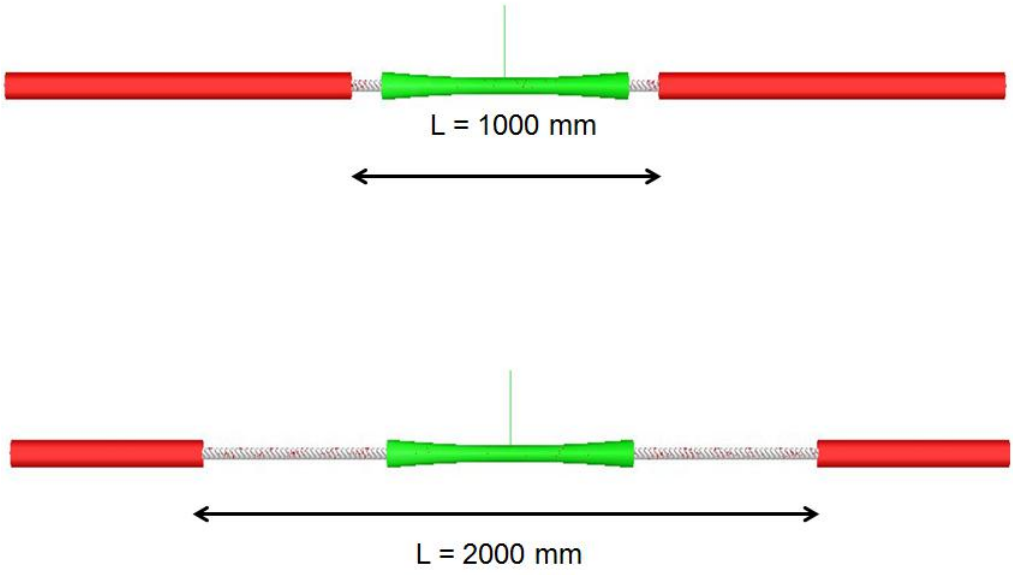

Figure 26: Two different FE models of copper conductors based on variation of model length and number of elements.

1. The axial stiffness correlation as shown in Figure 27.
2. The fact that all fatigue failures were found in the 2^{nd} and 3^{rd} layers.
3. Visual observation of the specimen, indicating gaps between the wires within the 3^{rd} and outermost layers.
4. Numerical stability.

The associated stick-slip parameters are given in Table 4.

The point contact force distribution due to maximum tensile load 30000 N is shown in Figure 28. The point contact forces show that the quantities are nearly similar over the model length except close to the end fittings. The average point contact forces indicating -43.6 and -21.8 N, respectively, located between 2^{nd} and 3^{rd} layers and between 3^{rd} and 4^{th} layers.

The distribution of the inline contact forces within layers and 1^{st} (centre) and 2^{nd} layer are compared in Figure 29. The results demonstrate that the inline contact force distribution within 2^{nd} layer is almost similar to the inline

Table 3: Contact calibration factors for inline (C_{in}) and point contact (C_{po}) based on Eqs. (10) and (11), respectively.

Type of contact	Located	Contact calibration factors
Inline contact	Between centre wire and 2^{nd} layer	4.86 10^{-5}
	Within 2^{nd} layer	4.86 10^{-5}
	Within 3^{rd} layer	5.5 10^{-7}
	Within 4^{th} layer	3.84 10^{-7}
Point contact	Between 2^{nd} and 3^{rd} layers	2.7 10^{-2}
	Between 3^{rd} and 4^{th} layers	2.1 10^{-2}

Table 4: Detailed contact parameters of 300 mm^2 full cross-section copper conductor.

Interface	Contact forces (average)	Nominal stiffness per interface	Stick-slip stiffness per interface (Eq. (7) [17])	Slip parameters $[mm]$ (Eqs. (13) and (14) [17])
centre wire-2^{nd} layer	4.43 N/mm	100 N/mm^2	1564/mm^2	5.66 10^{-4}
2^{nd} layer-2^{nd} layer	4.43 N/mm	100 N/mm^2	1564 N/mm^2	5.66 10^{-4}
3^{rd} layer-3^{rd} layer	0.05 N/mm	0.1 N/mm^2	1333 N/mm^2	7.50 10^{-6}
4^{th} layer-4^{th} layer	0.035 N/mm	0.1 N/mm^2	1218 N/mm^2	5.75 10^{-6}
2^{nd} layer-3^{rd} layer	43.6 N	903 N/mm	1.588 10^4 N/mm	5.5 10^{-4}
3^{rd} layer-4^{th} layer	21.8 N	1411 N/mm	3.33 10^4 N/mm	3.2 10^{-4}

contact force between centre and 2^{nd} layer where the average inline contact force is -4.43 N/mm. The inline contact force occurring within 3^{rd} layer is approximately -0.05 N/mm.

The smallest inline contact force is found to be within outermost layer, approximately -0.03 N/mm. This is a result of the reduced C_{in} defined in Table 3. The reduced inline contact forces in the 3^{rd} and outermost layers

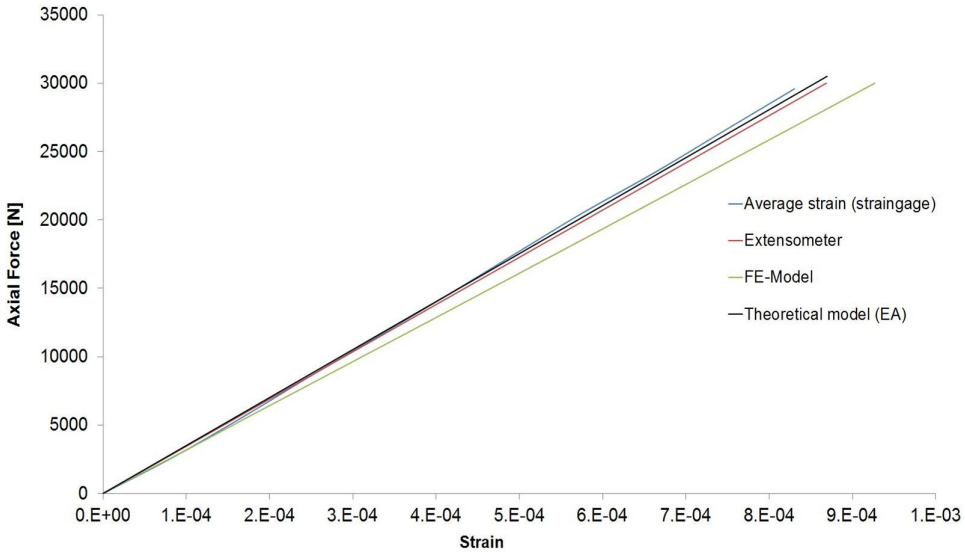

Figure 27: Comparison results of axial force vs. strain obtained from calibration tests, FE and theoretical model for 300 mm^2 copper conductor.

take an important role for increasing the friction forces on the contact surface of inner wires and causing the longitudinal stress range to be larger. Consequently, the predicted first fatigue failure was found to occur in the 2^{nd} layer.

The axial force distributions of individual wires for the different layers is presented in Figure 30. The highest axial force occurred in the centre wire with 836 N. For the 2^{nd} wire the axial force is 822 N. For the 3^{rd} and 4^{th} wires the axial forces are 812 N and 795 N, respectively, which demonstrates almost equal sharing of axial load between layers.

5.2. Tension-Bending Fatigue

The curvature along the model at maximum deformation is shown in Figure 31 for both radii of curvature 3000 and 6500 mm with different model lengths. The curvature is essentially unaffected by model length.

Figure 32 shows that the end beams were applied to simulate the die springs by associating the same axial stiffness and then introducing a pretension of 30000 N as indicated at point S. Further, a conductor model was exposed to constant reversed bending loads in the mid-span. The reversed bending loads induce dynamic axial forces histories acting at end beams of

the model. The maximum dynamic forces are 31.5 and 30.5 kN for radii of curvature 3000 and 6500 mm, respectively.

Figures 33 presents the longitudinal stress versus curvature hysteresis loop during reversed bending for radius of curvature $\rho_1 = 3000\ mm$ taken from 2^{nd} layer. The hysteresis loop corresponds to the frictional energy dissipated at the contact interfaces. The maximum longitudinal stress range is approximately 260 MPa as compared to 122 MPa only considering pure bending (see Figure 17).

Figure 34 presents the predicted maximum longitudinal stresses with respect to the hysteresis loop for radius of curvature $\rho_2 = 6500\ mm$ taken from 2^{nd} layer. The predicted maximum longitudinal stress range ($\Delta\sigma_{xx}$) is approximately 183 MPa as compared to 56 MPa only considering pure bending (see Figure 17).

The details of stress contributions to the predicted longitudinal stress range for both radii of curvature are summarised in Table 5. It is seen that the friction stress is providing the largest contribution to the maximum longitudinal stress range for both radii of curvature, 113 MPa in the 2^{nd} layer. The stress range of friction stress obtained from the analytical model given in Eq. (7) is 117 MPa. The predicted localised bending stresses for both radii of curvature gives an increase of approximately 12% compared to the analytical bending stress.

The predicted fatigue damage distribution in the 2^{nd} layer is displayed in Figure 35 for radius of curvature 3000 mm. The figure shows that the predicted first fatigue failure would occur within the bellmouth. This is in accordance with the observed fatigue failures seen in the tests. The predicted number of cycles to failure is 1.35 10^5 cycles.

For radius of curvature of 6500 mm, the predicted fatigue damage distribution is displayed in Figure 36, the predicted first fatigue failure located at 2^{nd} layer inside the bellmouth. The estimated fatigue life is 2.40 10^6 cycles.

Mesh sensitivity studies were performed by doubling the number of elements and the model length. No significant differences in results were noted.

6. Discussion of Results

The bending tests of the 300 mm^2 conductor were analysed by the calibrated FE model. The aim of the analysis was to validate a fatigue prediction model, based on S-N data for individual wires tested in tension-tension. In

Table 5: Summary of stress contribution to the predicted actual longitudinal stress range for radii of curvature $\rho_1 = 3000$ and $\rho_2 = 6500$ mm.

$\rho_1 = 3000$ mm	Contribution	Analytical formulation [MPa]	FE Analysis [MPa]
	Die spring	8	8
	Friction	117	113
	Bending stress in the -y direction	122	139
	Total	247	260
$\rho_2 = 6500$ mm			
	Die spring	5	5
	Friction	117	113
	Bending stress in the -y direction	56	65
	Total	178	183

the FE model effects of slip, friction, contact forces and local bending were taken into account.

In all the load cases that were analyzed the model predicted the first fatigue failures to take place in the 2^{nd} layer of the conductor wires, inside the bellmouth. This is in agreement with the full scale tests, where failures were located to the 2^{nd} and 3^{rd} layers. The reason why the interior layers of wire tend to have the shortest fatigue life is the contribution to dynamic stress from frictional forces acting on both sides of each layer.

The same tests were analysed by the analytical model presented in Section 3. This model does not account for local bending of the wires in a stranded conductor. However, as seen from Table 5 the results for the stress analysis is in good agreement with the FE model. The reason for the agreement is that in this case the contribution from local bending to dynamic stress was relatively small (approximately 12%).

In Figure 37 the main results of the study are summarized in terms of S-N data. The scatter band shows the S-N data for individual wires tested in tension-tension, corrected for stress concentrations due to plastic deformation of the wires from the compacting process. The S-N data plotted in terms of

nominal stress (Eq. (2)) for 300 mm^2 conductors tested in the bending rig are seen to fall far below the scatter band. The reason for the discrepancy is the effect of frictional forces and local bending, which are neglected in the elementary beam model. When plotted in terms of maximum stress range calculated by the FE model, all the data points with one exception fall within the scatter band. This demonstrates the significance of the contributions from frictional forces and local bending in the prediction of fatigue strength of copper conductors.

The fatigue lives calculated on the basis of the analytical model in the same fall in the same within the scatter band.

The coefficient of friction plays a key role in the fatigue performance of the copper conductor since it effects the longitudinal stress range. The predicted fatigue lives of lubricated conductor model ($\mu = 0.02$) fall below the scatter band. The longitudinal stress σ_{xx} increases when the coefficient of friction increases. Increasing the coefficient of friction to $\mu = 0.1$ brings the data points within the scatter band, suggesting that the effect of lubrication was not constant during the test. The latter may also explain the fact that the predicted stress range only partially lifts the test data into the scatter band of S-N data for individual wires. However, noting the fact that the unlubricated results for the 6500 mm radius case also fall to the left side of the scatter band indicates that other load condition specific effects such as fretting may contribute to the fatigue process as well.

The results further suggest that the best fit fatigue estimate is found by assuming no inline contact within the outer layers and in that case the analytical model and the FE model give essentially the same results for fatigue prediction of stranded conductors.

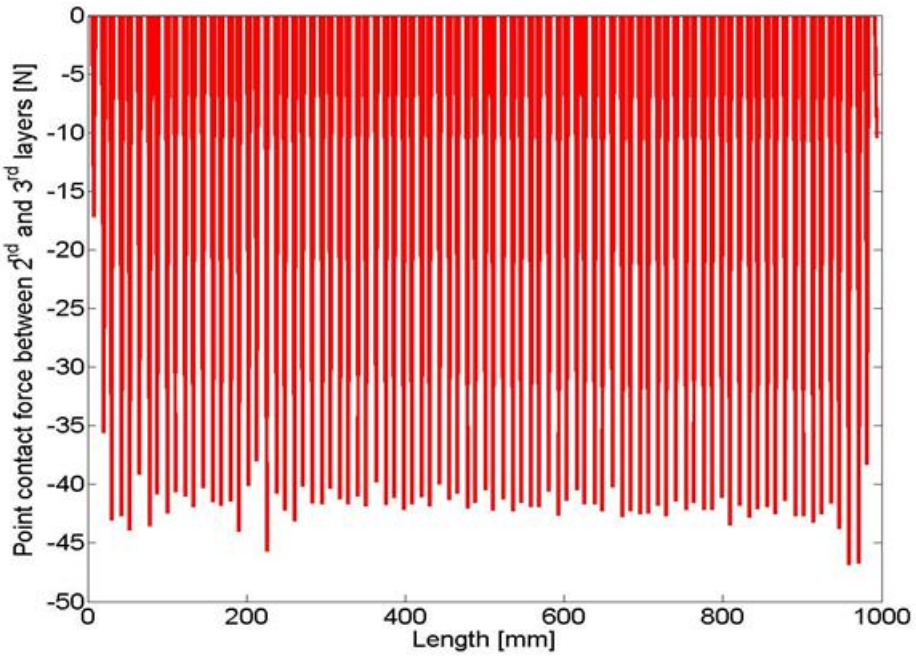

(a)

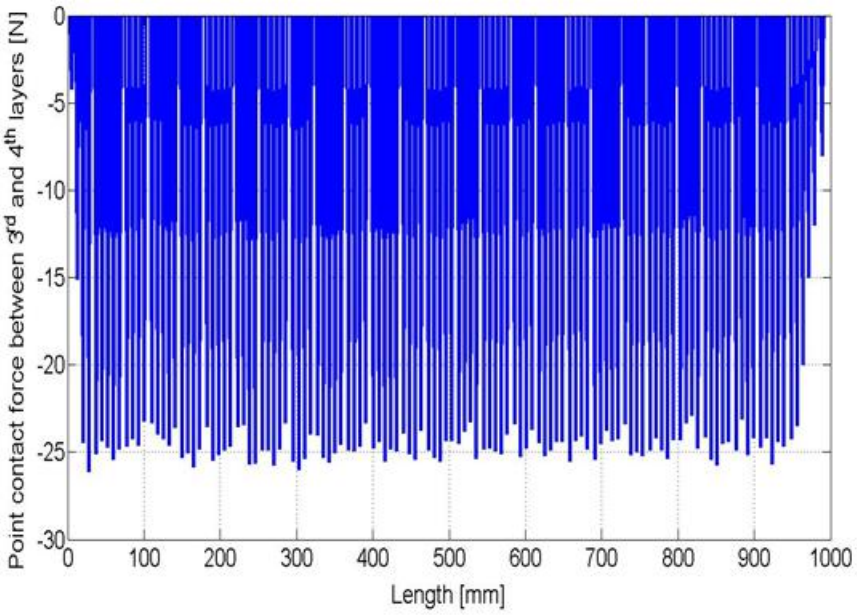

(b)

Figure 28: Point contact distribution occurring in adjacent layers due to tensile load 30000 N. (a) Between 2^{nd} and 3^{rd} layers. (b) between 3^{rd} and 4^{th} layers.

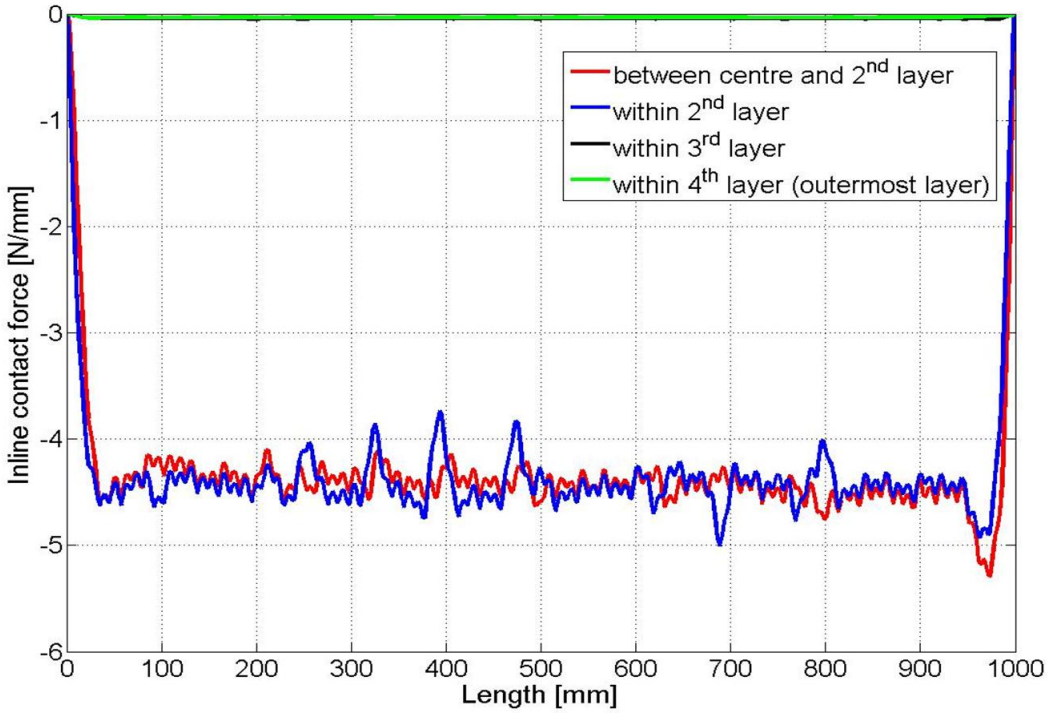

Figure 29: Inline contact distribution within layers and between centre and 2^{nd} layer due to tensile load 30000 N.

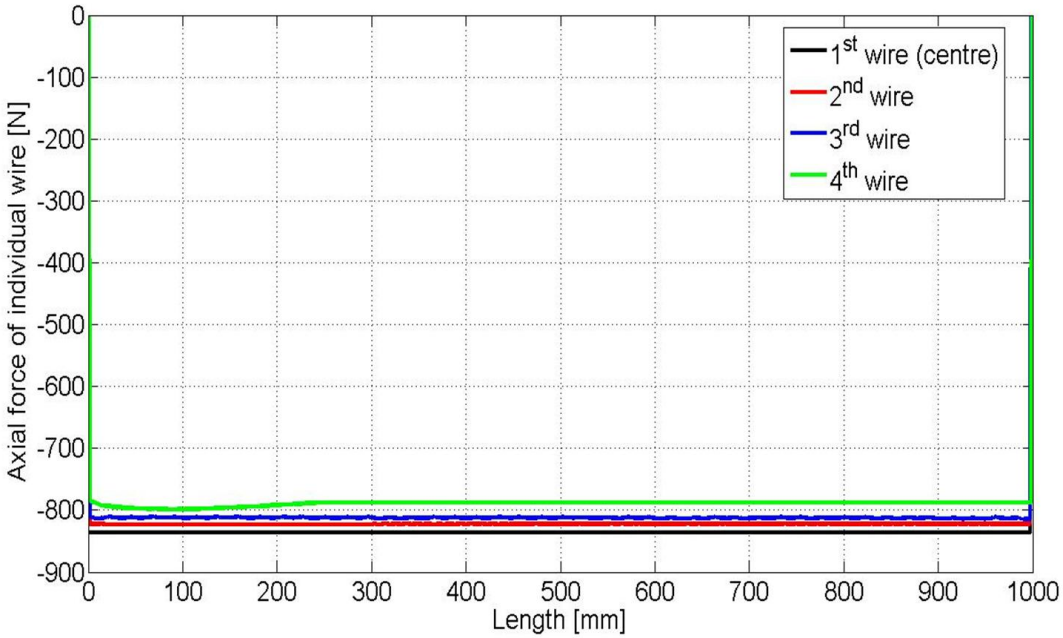

Figure 30: Axial force distributions of individual wires from different layer due to tensile load 30000 N.

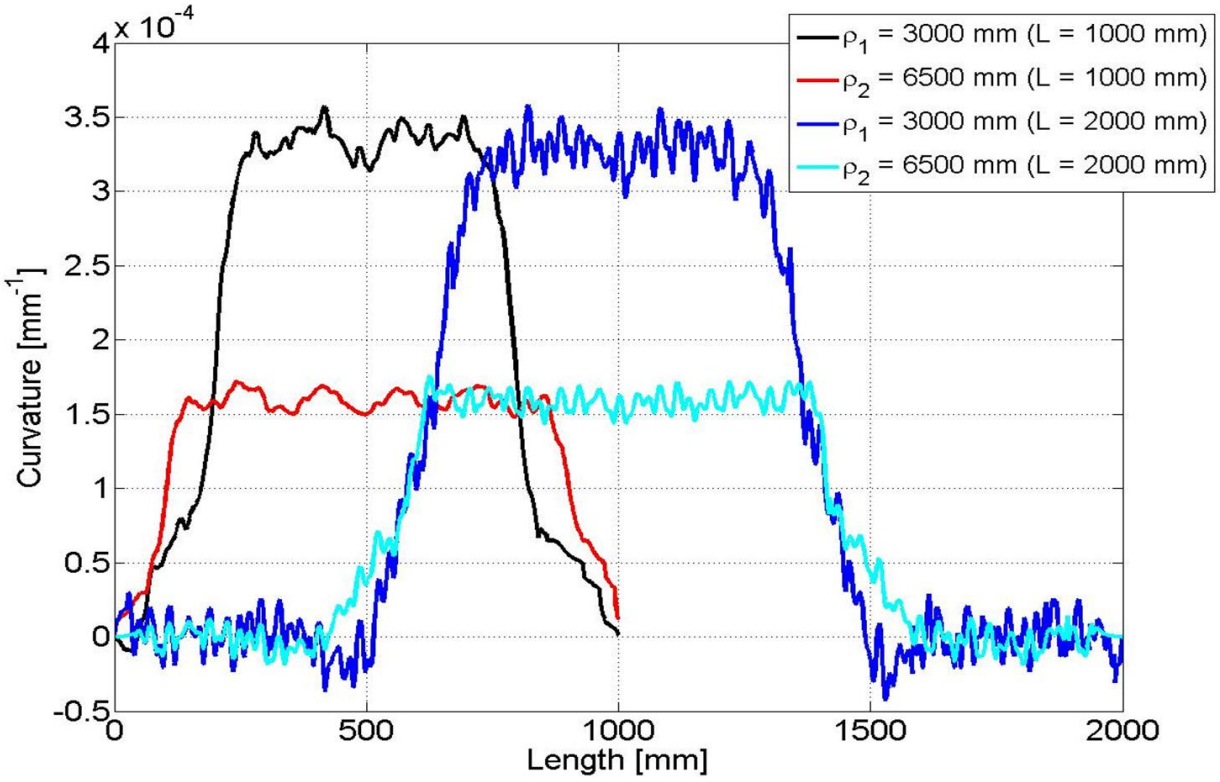

Figure 31: Bending curvature along the model at maximum deformation including different model length (L) and radius of curvature (ρ).

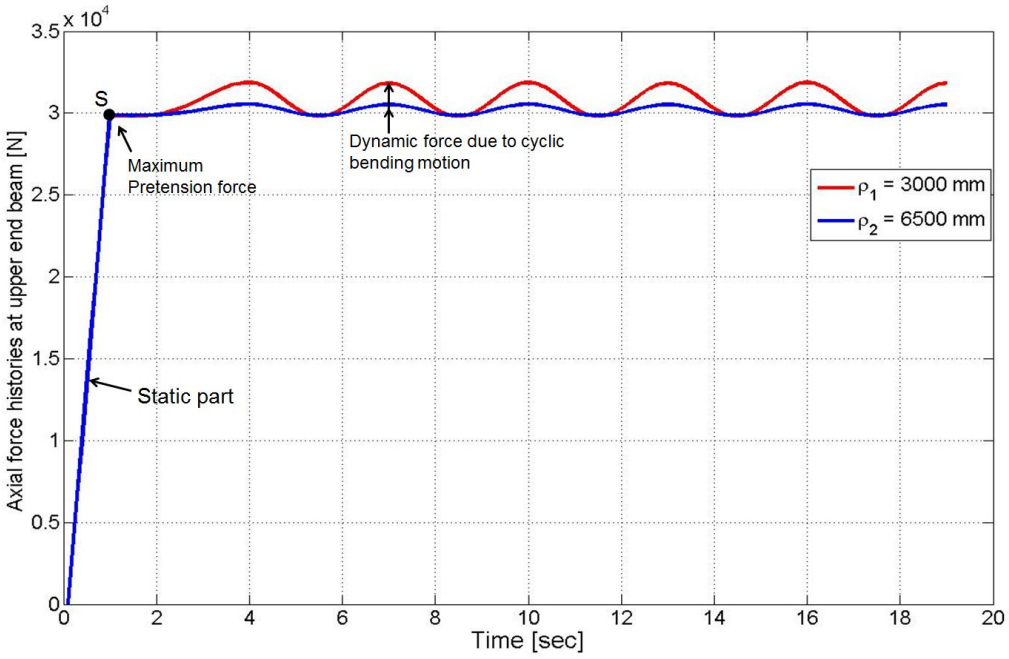

Figure 32: Axial force histories acting at end beams due to reversed bending loads.

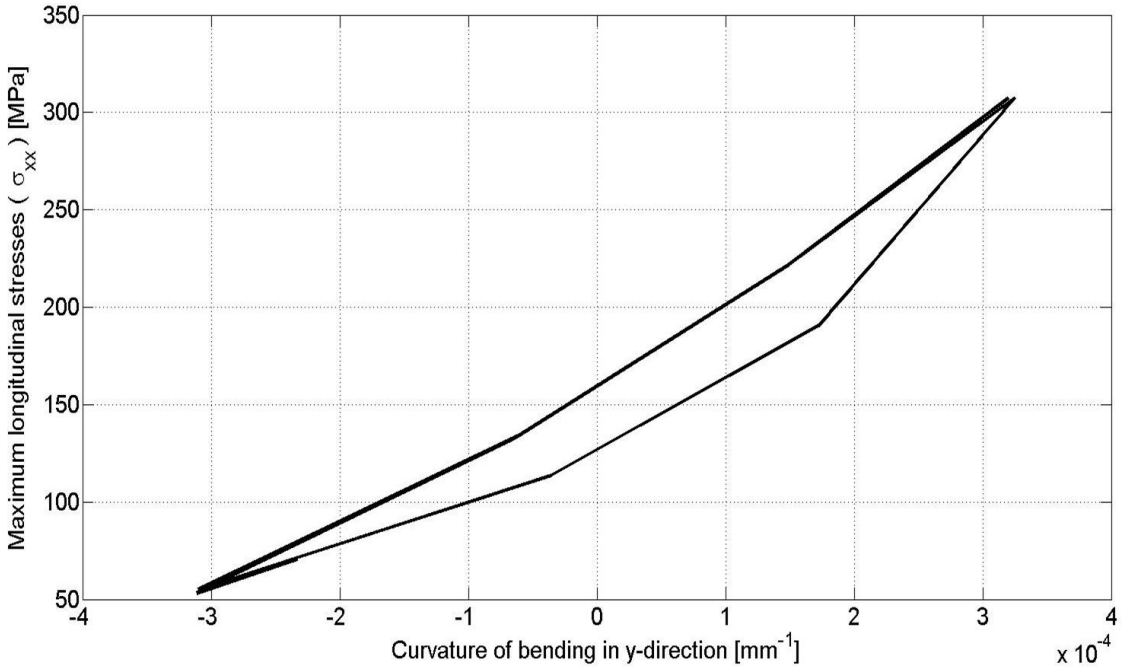

Figure 33: Predicted maximum longitudinal stress vs. curvature hysteresis loop due to reversed bending in the 2^{nd} layer at the location of maximum fatigue stress for radius of curvature $\rho_1 = 3000\ mm$.

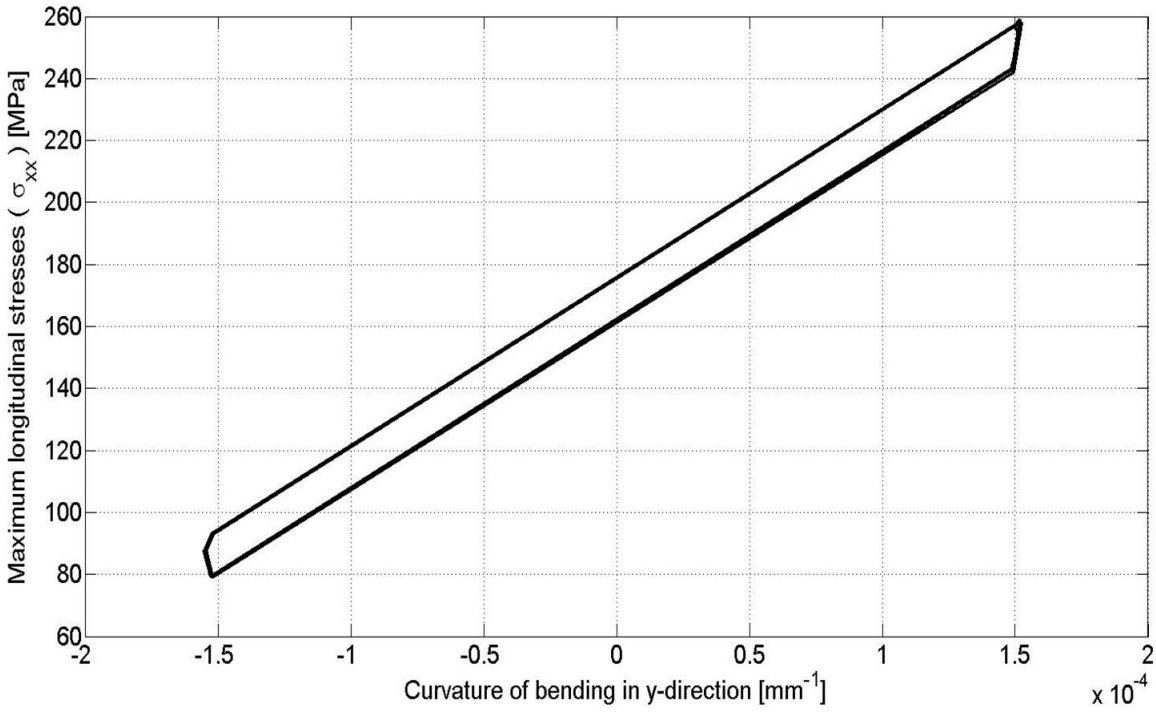

Figure 34: Predicted maximum longitudinal stresses vs. curvature hysteresis loop due to reversed bending motions at the location of maximum fatigue stress for radius of curvature $\rho_2 = 6500\ mm$ in the 2^{nd} layer.

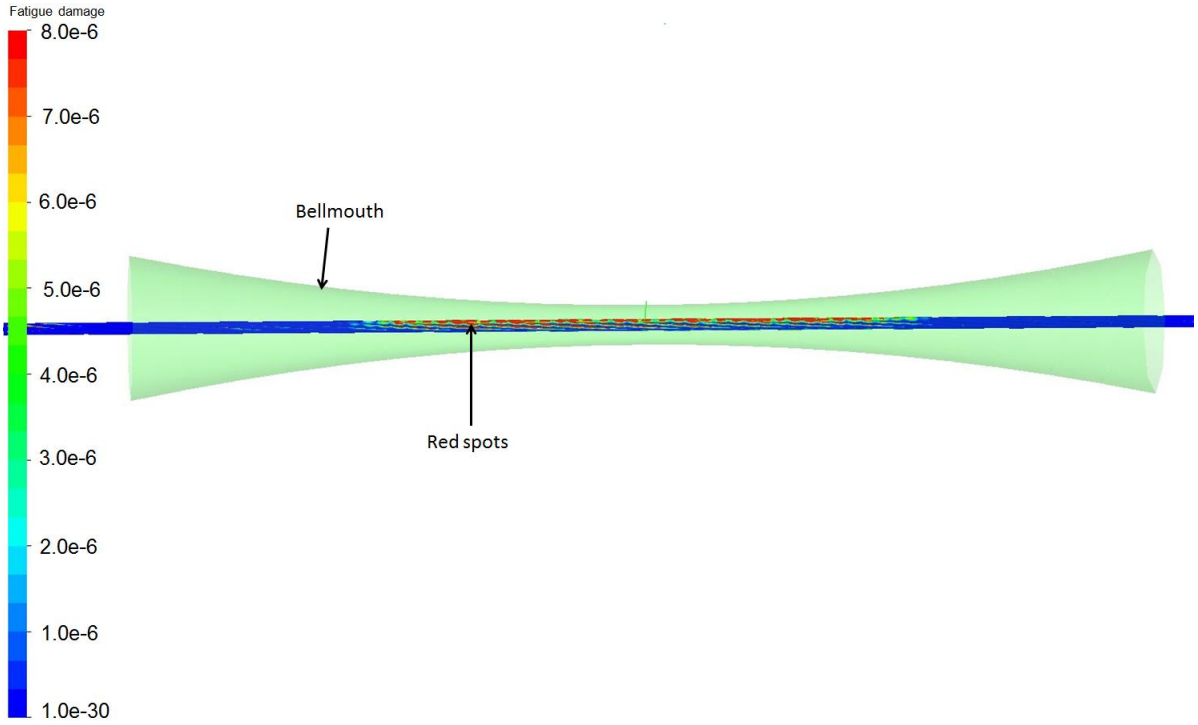

Figure 35: Predicted fatigue damage distribution in the 2^{nd} layer full cross-section conductor model due to reversed bending with radius of curvature $\rho_1 = 3000\ mm$.

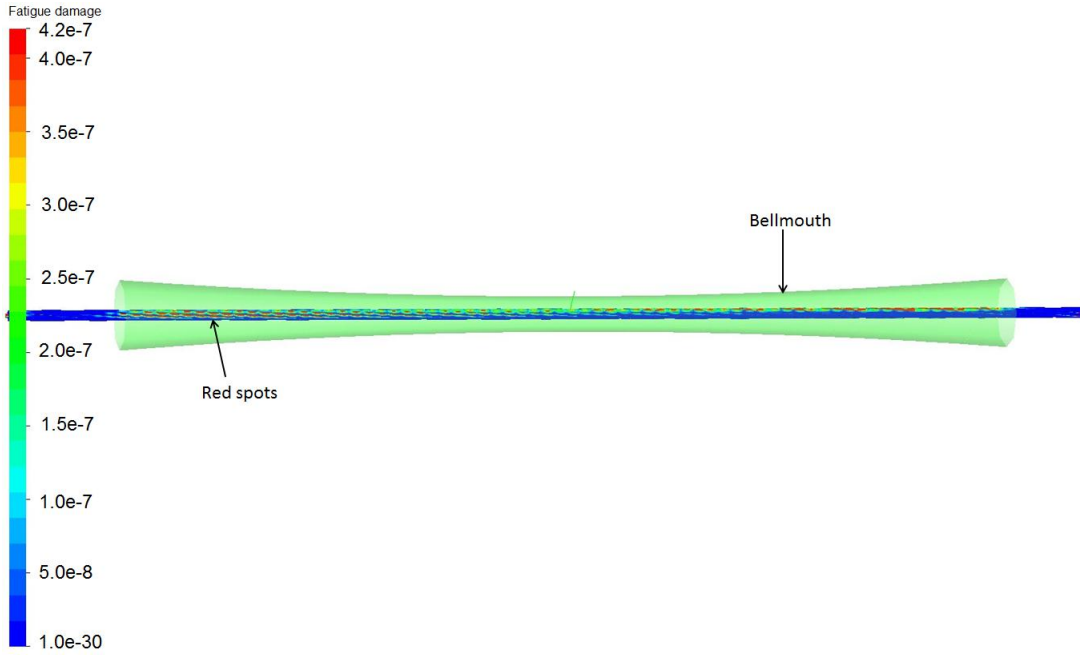

Figure 36: Predicted fatigue damage distribution in the 2^{nd} layer full cross-section conductor model due to reversed bending with radius of curvature $\rho_2 = 6500\ mm$.

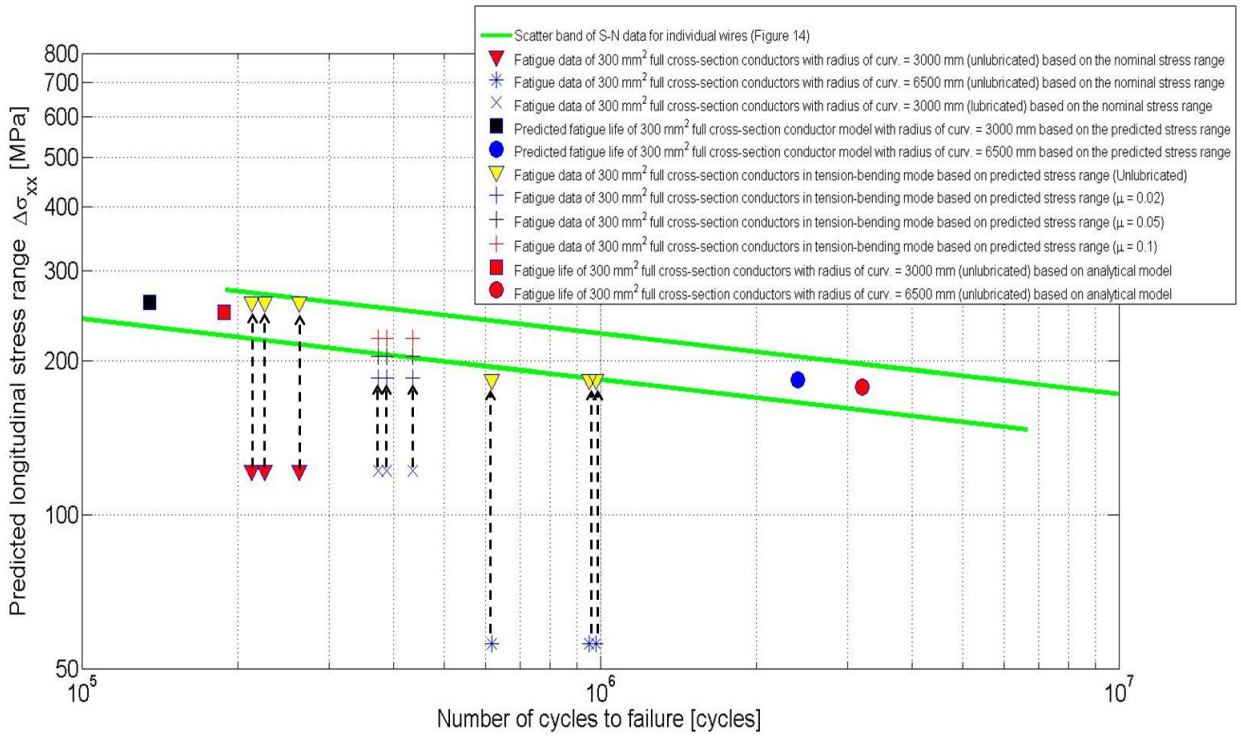

Figure 37: Predicted fatigue life of 300 mm^2 conductor using various models, based on S-N data for individual wires taken from 95 mm^2 and 300 mm^2 conductors displayed in Figure 14

.

7. Conclusions and Suggestions for Future Work

The fatigue mechanisms and fatigue strength of stranded copper conductors subjected to static tension and reversed bending loading were investigated. A finite element model was developed and validated for fatigue strength prediction based on S-N data from individual wires tested in tension-tension loading. The model is based on beam and beam contact elements, where a simplified contact modelling procedure was adopted. Coefficient of friction was obtained by calibration to test data. The following conclusions are drawn from the study.

1. S-N data of individual wires were taken from 95 mm^2 and 300 mm^2 conductors and tested in tension-tension loading. When analyzed and plotted in terms maximum stress due to stress concentrations from geometric irregularities, the data were found to fall within a common scatter band.
2. Full scale copper conductors were fatigue tested in a specially designed rig with constant tension and reversed bending loading. Analyzing the test data using nominal stress from elementary beam theory gave S-N data significantly lower than the scatter band from testing of individual wires.
3. When analyzing the full scale data with the FE model, good agreement was obtained with the S-N curve for individual wires tested with tension-tension loading. For the fatigue life ranges investigated in this study, the FE model was thus validated as a model for fatigue strength prediction of full scale conductors, based on fatigue strength of individual wires.
4. The full scale tests showed that lubricated conductors have a longer fatigue life than unlubricated conductors. The reason appears to be that lubrication reduces friction between wires, and hence leads to reduced dynamic stresses.
5. Fractography of wires from full scale tests showed that fatigue initiation took place from trellis contact areas. No indication of fretting was found. However, the results presented here do not rule out the possibility that fretting may have an effect. Full scale tests at relatively long lives tended to fail earlier than predicted by the model, indicating some contribution to the fatigue damage from fretting.
6. Calibration tests are required to calibrate coefficients for calculation of frictional forces between layers of wire in a conductor.

7. An analytical model was developed for stress calculations. Effects of friction were included, but local bending of the wires was not. Good agreement with the FE model and the test data was obtained, due to the fact that in this case local bending accounts for a relatively small contribution to dynamic stress.
8. FE analysis of the full scale tests showed that wires in the 2^{nd} layer had the shortest fatigue life. In the full scale tests, all broken wires were found in the 2^{nd} and 3^{rd} layers. The reason why the inner layers have shortest fatigue life is the contribution from friction forces to the dynamic stress.
9. With the numerical model, in order to obtain a best fit (see Figure 37 it was necessary to assume a small hoop stiffness. This is similar to the analytical model that only consider radial transformation of forces, however, including the same physical behavior in terms of elastic bending and friction. This suggests that for cases with small local bending the fatigue performance of the copper conductors can be described by a simple analytical model.

Further studying will focus on investigating the fatigue of full cross-section copper conductors with various geometrical cross-sections and for larger fatigue lives to quantify the importance of fretting effects.

Acknowledgement

The authors acknowledge ABB, Karlskrona, Sweden for providing test materials applied in the test. The laboratory personel at the NTNU Marine Technology Center Structural Laboratory is also acknowledged for assistance related to the testings. The authors also want to acknowledge Dr. Janne Gjøsteen for valuable support related to the Uflex3D software.

[1] Mindlin, R.D., 1949, Compliance of Elastic Bodies in Contact, Journal of Applied Mechanics, **71**, 259 - 268.

[2] Dong, R.G., and Steidel, F. R., Jr., Contact stress in stranded cable, Experimental Mechanics, **5**(5), 1965, 142-147.

[3] Johnson, K.L., Contact Mechanics, 1985, Cambridge University Press.

[4] Raoof, M. and Hobbs, R.E., Analysis of Multilayered Structural Strands., Journal of Engineering Mechanics, **114**, 1988, 1166-1182.

[5] Raoof, M., 1989, Axial Fatigue of multilayered strands, Journal of Engineering Mechanics **116**, 2083-2099.

[6] Raoof, M., 1991, Axial fatigue life prediction of structural cables from first principles. Proceedings Institution of Civil Engineers, **91**;19-38

[7] Raoof, M., and Huang, Yu Ping., Cyclic bending characterisitcs of sheathed spiral strands in deep water., International Journal of Offshore and Polar Engineering, **3**, 189-196, 1993.

[8] Hobbs, R.E. and Raoof, M., 1994, Mechanism of fretting fatigue in steel cables, International Journal of Fatigue, **16**, 273-280.

[9] Zhou, Z.R., Cardou, A., Fiset, M. and Goudreau, S., 1994 Fretting fatigue in electrical transmission lines., Wear, **173**, 179-188.

[10] Zhou, Z.R., Cardou, A., Goudreau, S., and Fiset, M., 1996, Fundamental investigations of electrical conductor fretting fatigue, Tribology International, **29**, 221-232

[11] Papailiou, K. O., 1997, On the Bending Stiffness of Transmission Line Conductors., IEEE Transactions on Power Delivery, **12**.

[12] Hong, K-J., Der Kiureghian, A., and Sackman, J. L., Bending Behavior of Helically Wrapped Cables., 2005, Journal of Engineering Mechanics, **131**.

[13] Karlsen, S., Slora, R., Heide, K., Lund, S., Eggertsen, F., Osborg, P. A., Dynamic Deep Water Power Cables., 2009, RAO/CIS Offshore.

[14] Karlsen, S., 2010, Fatigue of copper conductors for dynamic subsea power Cables, Proceedings of the OMAE 2010 29th International Conference on Ocean, Offshore and Arctic Engineering, Shanghai, China.

[15] Paradis, J-P. H., Legeron, F., Modelling of the free bending behavior of a multilayer cable by taking into account the tangential compliance of contact surfaces., 2011, Proceedings of 9^{th} International Symposium on Cable Dynamics (ISCD), Shanghai, China.

[16] Nasution, F.P., Sævik, S., Gjøsteen, J.K.Ø. and Berge, S., Experimental and Finite Element Analysis of Fatigue Performance for Copper Power Conductor, International journal of fatigue, **47**, 2013, 244-258.

[17] Nasution, F.P., Sævik, S., Gjøsteen, J.K.Ø., Finite Element Analysis of the Fatigue Strength of Copper Power Conductors Exposed to Tension and Bending Loads., International Journal of fatigue., **59**, 2014, 114-128.

[18] Sævik, S., Theoretical and experimental studies of stresses in flexible pipes., Computers and Structures, **89**, 2011, 2272-2291.

[19] Sævik, S., On stresses and fatigue in flexible pipes., 1992, Ph.D Thesis at Department of Marine Structures, NTNU, Norway.

[20] Sævik, S., and Li, H., Shear interaction and transverse buckling of tensile armours in flexible pipes., Proceedings of the 32nd International Conference on Ocean, Offshore and Arctic Engineering, International Conference on Offshore Mechanics and Arctic Engineering, 2013, Nantes, France.

[21] UFLEX3D Version 1.0.1 Theory and User Manual